Journal of Materials Chemistry A

Elasticity-oriented design of solid-state batteries: challenges and perspectives

Journal:	*Journal of Materials Chemistry A*
Manuscript ID	TA-REV-02-2021-001545.R1
Article Type:	Review Article
Date Submitted by the Author:	25-Apr-2021
Complete List of Authors:	Ren, Yuxun; Vanderbilt University, Mechanical Engineering Hatzell, Kelsey; Princeton University, Mechanical and Aerospace Engineering; Princeton University, Andinger Center for Energy and Environment; Vanderbilt University, Mechanical Engineering

Journal Name

ARTICLE TYPE

Cite this: DOI: 00.0000/xxxxxxxxxx

Elasticity-oriented design of solid-state batteries: challenges and perspectives

Yuxun Ren,[a] and Kelsey B. Hatzell *[abc]

Received Date
Accepted Date

DOI: 00.0000/xxxxxxxxxx

Engineering energy dense electrodes (e.g. lithium metal, conversion cathodes, etc.) with solid electrolytes is important for enhancing the practical energy density of solid-state batteries. However, large electrode volumetric strain can cause significant fracture, delamination, and accelerate degradation. This review discusses transport and chemo-mechanical challenges associated with energy dense solid state batteries. In particular, this review focuses on summarizing work which provides design strategies for implementation on energy dense anodes and cathodes. This review further assesses the properties which impact the elasticity of inorganic solid electrolytes and inorganic/organic hybrid electrolyte. Finally, this review discusses the advanced characterization approaches for analyzing the coupled electrochemistry/transport/mechanical phenomena that occur at buried solid-solid interfaces.

1 Introduction

Conventional lithium-ion batteries (LIBs) are widely used in a range of applications from portable electronics to electric vehicles[1,2]. Conventional LIBs are comprised of current collectors, a liquid electrolyte, and intercalation-based electrodes. There is significant interest in replacing the liquid electrolyte with a solid electrolyte (solid state battery) to enable energy dense anodes (Si, Li metal, etc.) and to improve the overall safety of the battery[3,4]. In addition, to safety and energy density, solid-state batteries may enable bipolar stacking, which can greatly reduce the battery stack volume and improve volumetric energy density[5,6].

Solid-state batteries typically consists a planar layered structure comprised of an anode, cathode, and a solid electrolyte separator (Fig. 1a). The cathode is a composite material which combines the carbon/binder additive, the solid electrolyte, and the active cathode material. The composite solid microstructure enables effective ion and electron transfer for maximum material utilization. With intensive development in recent years, the performance metrics of solid-state batteries with intercalation-type graphite anodes and layered oxide cathodes are similar to conventional LIBs (200 Wh kg^{-1}, based on the cell mass)[7,8]. Given these excellent results, there is significant interest in increasing the energy density of a solid-state battery via integrating energy dense anodes and cathodes. There is widespread interest in lithium alloys (silicon, tin, germanium) and lithium metal anode as promising alternatives to graphite. Furthermore, energy dense conversion-type cathodes such as sulfur or iron fluoride can potentially replace the layered oxide (Fig. 1b)[9]. However, energy dense electrode materials suffer from high volumetric strain during electrochemical cycling and can result in cracking or fracture (Fig. 1c)[10,11,12]. Advanced electrode design is necessary to prevent the chemo-mechanical failure[7]. This problem becomes exacerbated in solid-state systems. Solid state systems lack a liquid or soft phase that can accommodate stress- and strain- distributions. As a result, localized regions with high stress can manifest at the electrode|electrolyte interface and cause solid electrolyte fracture[13–16]. Thus, solid state energy storage design requires electrodes that can effectively distribute stress between individual solid state components (e.g. electrode and electrolyte). Design of electrode geometries requires exquisite control over chemical (transport) and mechanical properties across multiple length scales.

The complex nature of chemo-mechanical transformatiosn at electrode|solid electrolyte interfaces makes it challenging to identify specific material properties to design for. Instead, predicting material system and microstructure properties that lead to long cycle lifetime may be necessary. For instance, anode design for solid state batteries may look very different for lithium metal and a lithium alloy. Lithium metal can undergo an infinite volume change during cycling. Microstructural anisotropy in both the solid electrolyte and electrode can lead to irregular lithium deposition/dissolution[15,22]. Therefore, 3D lithium metal architecture infiltrated with an inorganic solid electrolyte is challenging. Typically, solid-state batteries use pure lithium metal which requires a solid electrolyte film with adequate stiffness to accom-

[a]Department of Mechanical Engineering, Vanderbilt University, Nashville, TN, USA, 37240
[b]Department of Mechanical and Aerospace Engineering, Princeton University, Princeton, NJ, USA, 08540
[b]Andlinger Center for Energy and Environment, Princeton University, Princeton, NJ, USA, 08540; E-mail: kelsey.hatzell@princeton.edu

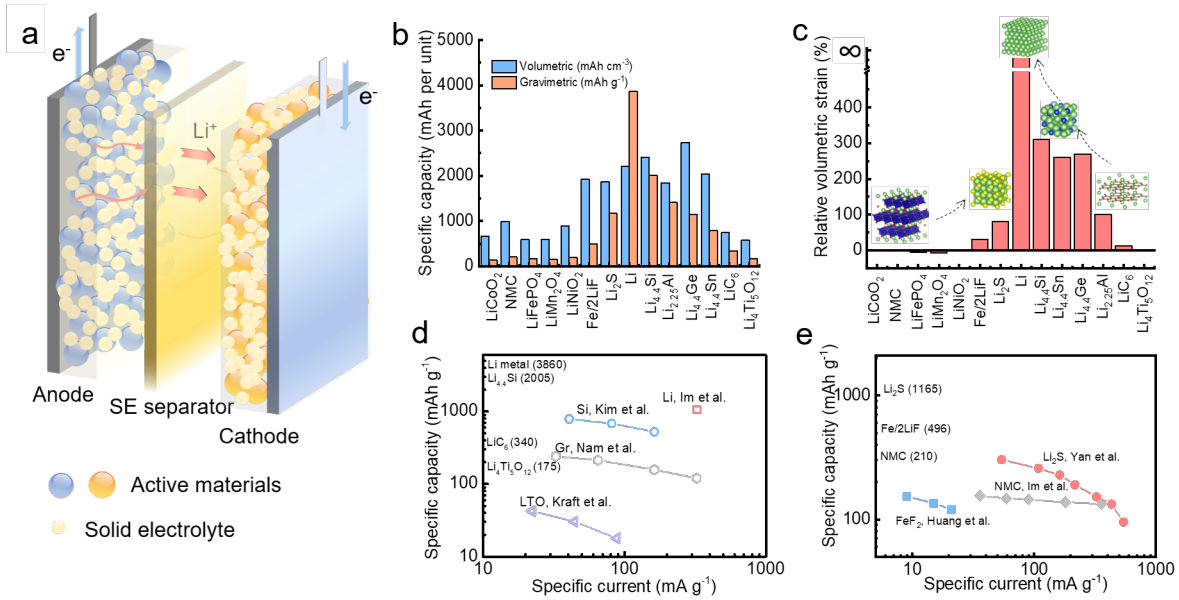

Fig. 1 Schematic operation principle of solid-state batteries. (a) Schematic operation principle of solid-state batteries. (b) Specific capacity and (c) volumetric strain of different types of cathode and anode materials. The green atom represents active lithium.(d, e) Specific capacity and current of solid-state anodes[17 18 16 19](d) and cathodes[17 20 21] (e). Gr is the abbreviation for graphite here. The calculation considered the entire weight of the electrodes. References can be found in Table 1.

modate that volume change and regularize lithium deposition and dissolution in the through-plane direction. Both rigid and soft solid electrolyte impact the formation of lithium filaments. A rigid solid electrolyte can uniformly apply a compressive stress to flatten the plated Li, while the soft, elastic solid electrolyte prevents the local protrusion by applying a higher local stress[3,4]. Alloy functions as the host for lithium and exhibits a high volumetric strain (e.g. 300% for the lithiation of silicon). Expansion of alloy particles inside the electrode can stretch and shear the solid electrolyte matrix significantly, and thus it may be advantageous to have a porous electrode structure and a rigid and tough solid electrolyte. Under the rigid constraint of solid electrolyte, the alloy can expand and constrict within the local region with a smaller level of interfacial stress. Conversion cathodes experience a smaller volumetric strain, but suffer from poor transport properties. Thus, softer and more elastic solid electrolytes might be necessary to ensure effective contact between different material phases for electron and ion transport.

Thus, there is a wide array of interactions that need to be considered for solid state batteries design. Given the complexity in designing high-strain electrodes, there is a huge gap between the practical capacity and the theoretical capacity of the electrode materials (Fig. 1d,e). This gap becomes even more apparent in material that exhibit high strain. This review focuses on challenges and approaches for the application of high-strain electrode materials in the solid-state batteries. Section 2, 3 and 4 discusses transport and mechanical challenges and impact on electrode design. Special attention is focused on high-strain materials (e.g. Li alloy, Li metal, and conversion materials) (Fig. 2). Section 5 and 6 discuss the design approaches for rigid inorganic solid electrolyte with a high stiffness and soft inorganic/polymer hybrid electrolyte with a high elasticity. Section 7 summarizes the characterization techniques for the mechanical properties and coupled electrochemistry/mechanics/transport phenomena. Theoretical approaches for multi-scale modeling is also briefly discussed. Finally, the review concludes by discussing the overarching challenges and opportunities associated with mechanical design of solid state batteries.

Fig. 2 Design strategies for the solid-state high-strain electrodes.

2 Elasticity design for alloy anode

2.1 Transport and mechanical challenges for alloy

Alloy anodes, such as silicon, germanium, and tin are examples of promising alternatives to graphite in solid-state batteries. Silicon (Si) possesses the highest gravimetric energy density (2005 mAh

$g^{-1}_{Li4.4Si}$) [23] and in a fully lithiated state, one Si atom can alloy with 4.4 Li atom

$$Si + 4.4e^- + 4.4Li^+ \rightarrow Li_{4.4}Si \quad (1)$$

Si exhibits a relatively low ionic conductivity but a reasonable electronic conductivity (after doping) of 10^{-2} S cm^{-1}. The transport properties of lithiated silicon (Li_xSi) are fairly good with an electronic conductivity of 1 S cm^{-2} and Li^+ diffusivity of 10^{-13}-10^{-12} cm^{2}s^{-1} (depending on the Li concentration). These properties are comparable with lithiated graphite (10^{-11} cm^{2}s^{-1}) [24 25 26 27]. Similar to graphite, lithiated silicon acts as mixed ion and electron conductor and can achieve complete lithiation when using micron-sized Si particles with a liquid electrolyte [28].

While Si demonstrates excellent capacities and reasonable transport properties, mechanical degradation during repeated lithiation/delithiation accelerates capacity decay. Si can experience a 300% volumetric strain during lithiation (based on $Li_{4.4}Si$), which result in the cracking and fracture. Lithiation-induced stress can impact both charge transfer and transport properties. In addition, the stress generated in the Si particles can impact local mechanical properties in the solid electrolyte matrix. Table 1 summarizes representative solid-state Si anode performance properties. Solid-state Si anodes demonstrate lower performances in comparison to intercalation-type graphite or $Li_4Ti_5O_{12}$ in terms of the areal capacity and cycle life. Electrode design is necessary to overcome these chemo-mechanical transformations and improve cell-level performances. The theoretical origin of lithiation induced stress and impact on charge transfer and transport processes are detailed below.

2.1.1 Stress-dependent overpotential

Mechanics can play a significant role on charge transfer in solid-state Si anodes. Local constriction due to microstructure, semi-local constriction due to component interfaces, and intraparticle stress generation during lithiation and delithiation all lead to non-uniform mechanical responses. When a dense Si particle is being lithiated, the newly formed lithiated Si at the reaction front can impose a compressive stress on the lithiated Si shell, and push the lithiated shell outward. Previous studies reveal that when Si is imposed with a compressive stress, it requires an additional overpotential for the lithiation reaction to proceed [32 33]. The electrochemical reaction kinetics, at the stress-free state, follows the Butler-Volmer relationship. This relationship can be modified into the following form for a stress-state:

$$i = i_0(\exp((1-\alpha)\frac{\eta + p\Omega}{k_BT} - \exp(-\alpha\frac{\eta + p\Omega}{k_BT})) \quad (2)$$

where i_0 is the exchange current, $p\Omega$ represents the change of strain energy, p is the mean local stress, Ω is the partial volume of Li (volume change of Li_xSi during one Li atom insertion) and k_BT is the thermal energy (0.0258 eV) [10,34].

Si anodes with liquid electrolyte demonstrate weak mechanical interactions with the carbon/binder domain upon lithiation and delithiation (Fig. 3a). In contrast, a solid-state Si anode will experience strong mechanical interactions between the Si anode and solid electrolyte. The Young's moduli for an elastic sulfide solid electrolytes is between 10 to 30 GPa which comparable to the Young's moduli of Li_xSi (E=12 GPa for $Li_{15}Si_4$) [35]. Thus, as the particle expands, the rigid inorganic solid electrolyte matrix can impose a compressive stress on the particle, and retard the lithiation-induced expansion and lead to interfacial stress generation (Fig.3b). Once the strain energy exceeds a critical value (fracture toughness), cracking can occur in the solid electrolytes to release strain energy. Previous studies suggest that sulfide solid electrolyte material is likely to crack when the electrode particle expands by greater than 7.5 % [36–38]. The subsequent crack can grown inward and increases the transport resistance, as the ion transport path becomes more tortuous [39].

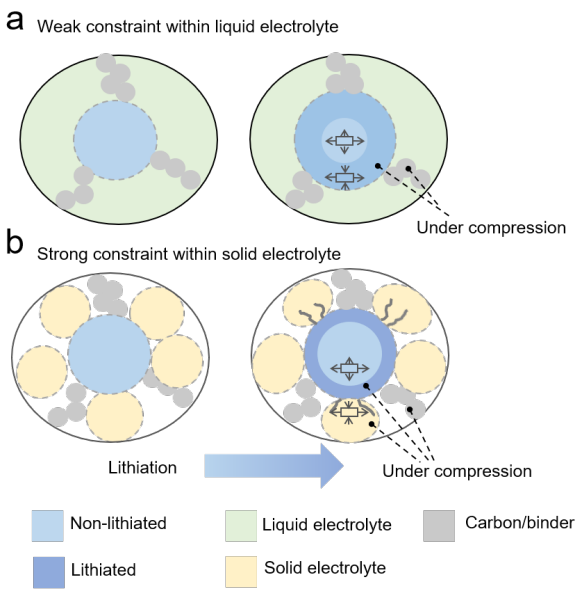

Fig. 3 Comparison of the lithiation process for a high-strain particle with weak constraint in liquid electrolyte, and strong constraint in solid electrolyte

2.1.2 Stress-driven transport

Lithiation-induced stresses can impact ion transport within the active material and between the electrode and solid electrolyte. During lithiation, the Li_xSi shell is under compression and the non-lithiated core is under tension. This results in an interfacial reaction between core and shell, which promotes ion transport to alleviate the stress [40]. This reaction is can be described as a diffusion process driven by the an ion concentration gradient. The correlation between the mean local stress and the diffusivity of a lithium ion is described by:

$$D = D_0 exp(\frac{p\Omega}{k_BT}) \quad (3)$$

where D_0 is the diffusivity at the stress-free condition; $p\Omega$ represents the change of strain energy, where p is the mean stress, Ω is the partial volume (volume change of sulfur during one Li atom insertion) and k_BT is the thermal energy (0.02582 eV). This relationship suggests that an electrode under a nominal stress can be spontaneously lithiated. In addition, this relationship also sug-

Table 1 Performance of the reported all-solid-state intercalation anode, and alloy anode.

Ref.	Electrolyte	Anode	AM loading (mg cm^{-2})	Weight ratio	Capacity (mAh cm^{-2})	Current (mA cm^{-2})	Retention/ Cycle number
Nam et al.[18]	Li_6PS_5Cl	Graphite	15.8	58.6%	3.5	0.15	100%/17
Kato et al.	LiI-Li_2S-P_2S_5	Graphite	51.3	46%	15	0.5	99%/10
Ito et al.[29]	Li_6PS_5Cl	Graphite	13.3	95%	3.8	0.143	91.7%/100
Kraft et al.[19]	LiI-LGPS	$Li_4Ti_5O_{12}$	45.5	50%	6.8	1.7	100%/50
Kim et al.[16]	Li_2S-P_2S_5	Si	1.0	40%	2.0	0.5	77%/20
Whitney et al.[30]	Li_2S-P_2S_5	Si-Sn	2.1	70%	2.2	0.168	95%/50
Whitney et al.[31]	Li_2S-P_2S_5	Sn	2.8	70%	2.8	0.28	80%/50

gests that non-uniform contact between the silicon active material and solid electrolyte can lead to non-uniform lithiation processes.

2.1.3 Stress-driven fracture and delamination

Solid-state Si anodes are susceptible to fracture, delamination and decomposition. Fracture of active material and solid electrolyte can be induced by either a high local stress that exceeds the fracture toughness of the material or a high local strain that exceeds the elastic strain limit. Poor interfacial adhesion within a composite electrode can lead to delamination during dynamic operation. Finally, electrode decomposition is possible if the electrode and electrolyte reside and dissimilar chemical potentials[41,42]. Recent work using electron microscopy techniques clearly demonstrated lithiation-induced fracture of at the outer surface of Si electrode upon lithiation[10,43]. During delithiation, the Li-rich core is under compression which can also lead to fracture[44] and at times delamination of the active Si electrode from the solid electrolyte matrix. Both mechanims have been experimentally verified via ex situ electron microscopy[45]. Ultimately, fracture and delamination can have a significant impact on the cycle lifetime of the solid-state Si electrode.

The mechanical properties of Si electrode particles play a significant role on stress distribution and ultimately failure mechanisms. Several recent studies have focused on tuning the particle size, electrode composition and operating pressure as a means to suppress fracture of Si particles[46]. During lithiation, small-sized silicon particles are more likely to undergo plastic deformation, which can suppress crack growth. Prior work on liquid electrolytes demonstrated that Si particles with diameters between 20 and 150 nm could be reversibly lithiated and delithiated[47]. Due to the complex mechanical interaction, nanosized dense Si particles (50 nm) combined with a solid electrolyte (Li_6PS_5Cl) demonstrated inferior capacity retention (91.3 % for 20 cycles)[16]. However, the cyclability is still visibly superior to the solid-state Si anode using 5-μm particles (73.9 % for 20 cycles)(Table. 1)[16]. Another approach to mitigate Si fracture is to tailor the ductility of the alloy active material. Coating Si with ductile alloys like Sn or Ge is one potential strategy. A Si-Sn alloy (Si:Sn=1:3 wt) with micron size particles demonstrated 80% capacity retention over 50 cycles when combined with a Li_2S-P_2S_5 solid electrolyte[30]. While the ductility of the active material can be effectively tailored via alloying, this strategy has not been shown to effectively mitigate fracture of the solid electrolyte matrix. Thus, the dynamic interactions between active material and solid electrolyte need to be carefully engineered to avoid fracture and promote long term cycling performance. This is especially important because solid electrolyte fracture can accelerate Si delamination. Previous studies used high stack pressure (70 MPa) to mitigate delamination[31,48]. However, the higher stack pressure can also make the lithiation more challenging by requiring a large overpotential (Equation (1))[34]. In terms of ease in operation and achieving uniform and constant overpotentials, it is desirable to cycle electrodes without reliance on a high stack pressure.

2.2 Electrode design for the alloy anode

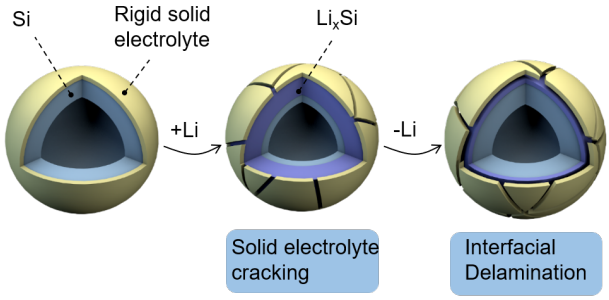

Fig. 4 Challenges facing the solid-state Si electrode using porous (hollow) Si.

Suppression of electrode volume expansion at the particle level is an ideal pathway toward improving the cycle lifetime and stability of solid-state Si electrodes. Volume expansion can be controlled via encapsulation and confinement. Most prominently, there has been several examples in conventional batteries with liquid electrolytes where a rigid shell was engineered around a porous Si electrode materials to suppress volume expansion[51–54]. One of the electrode designs, which is rather effective in liquid electrolytes, is the use of a hollow Si nanotube coated with a rigid Al_2O_3 shell[23]. The rigid shell induces a greater compressive stress in the hollow core during lithiation. Since the inner side of Si is stress-free, the reaction front easily pushes the non-lithiated core inward. The Al_2O_3 coating also prevents outward expansion of hollow Si and maintains direct contact between liquid electrolyte and Si. Such an electrode design enables limited volume expansion and long cycle lifetime. A similar design concept may be possible with solid-state electrodes.

A solid electrolyte matrix with a high Young's modulus can prevent outward expansion of the active material. However, delamination and solid electrolyte fracture are still possible[55,56]. During lithiation, the solid electrolyte matrix is under a compressive ra-

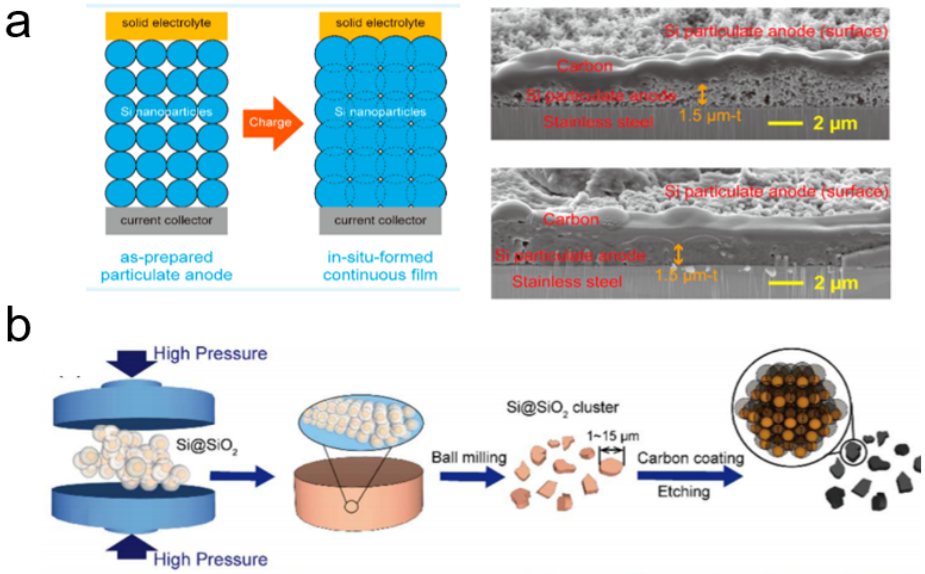

Fig. 5 Pressure-retardant electrode design for Si anode. (a) Schematic of a planar solid-state silicon anode. Cross-sectional SEM images of the as-prepared Si particulate anode and the anode in the fully charged state[49](Copyright 2020, American Chemical Society). (b) Schematic of a high tap density secondary silicon particle anode fabricated by scalable mechanical pressing for lithium-ion batteries[50] (Copyright 2018, Royal Society of Chemistry).

dial stress and tensile hoop stress. Both stresses increases during lithiation because there is a decrease in the stress-free surface as the reaction front moves inwards (Fig. 4). The circumferential stress should be greater and more destructive for thin-walled vessels that generally bear internal pressure. The build up of stress at the interface can initiate fracture on solid electrolyte. Nanoscale electrode coatings (Al_2O_3, TiO_2 and SiO_2) can potentially prevent fracture[57]. In addition to coating, improving the stiffness and toughness of the solid electrolyte may inhibit chemo-mechanical failure. Minimizing the presence of cracks and voids in the solid electrolyte matrix is key to inhibiting local high stress regions. In addition, strong adhesion between active materials and solid electrolytes is critical to avoid delamination which is likely during delithiation when both the solid electrolyte and silicon particles are under tension (Fig. 4).

Processing electrodes under high pressure can improve the density of the electrode and improve transport properties. Higher density electrodes can also improve the composite electrode's stiffness and facilitate an intimate contact between the Si particles and solid electrolyte matrix. However, silicon is intrinsically a brittle material and may not be able to sustain high pressures needed to achieve dense electrodes[56,58]. Previous studies demonstrate planar porous Si anodes can withstand stack pressures exceeding 120 MPa[41,49,59,60] (Fig.5a). The porous Si film was deposited on the current collector by spraying or sputtering. In comparison with the dense Si film, improved cyclability was observed when using porous Si as the anode. The challenge of this design however is its relatively low areal capacity (<3.0 mAh cm^{-2})[49,61] To enlarge the areal capacity, it is important to construct three-dimensional electrode by combining porous silicon electrode particles and rigid solid electrolytes. One approach to engineering silicon for high pressure is via creating rigid shells around micro-sized and/or nano-sized clusters of silicon particles. These clusters can create secondary silicon clusters. Prior work has employed hard (e.g. SiO_2 Fig. 5a) and soft (organic ligand Fig. 5b) templates to treat the Si nanoparticles and engineer an intrinsic porosity in the secondary clusters[50,62–64]. To obtain a microsized secondary cluster with internal voids, Si nanoparticles coated with a hard template ($Si@SiO_2$) can be first pelleted and then ball milled. This is followed by template etching and carbon coating[50]. Using soft template, Si can be directly assembled into microsized cluster[62]. To further enhance the mechanical stability, chemical vapor deposition of carbon or silicon was conducted on the particle's exposed surface. This templating approach enables silicon electrode which can sustain high compressive stress of 100 MPa. Additionally, Si nanoparticles can be dispersed onto a cellulose nanosheet, and the self-rolling of cellulose nanosheets during freeze drying can drive the formation of a topological microscroll[65]. The microscroll consists of controllable fraction of voids to accommodate volume expansion of Si, meanwhile, it can be deduced that the structure of microscroll is more robust than conventional nanostructure.

In brief summary, it is difficult to directly make the dense Si particle compatible with the solid electrolyte matrix, as the large stress induced by volume expansion requires a high lithiation driving force (overpotential) and leads to the solid electrolyte cracking. A potential solution is to combine the porous Si particle with a compatible solid electrolyte matrix. High density electrodes are necessary to achieve effective transport properties for electrodes. It is as critical to engineer the alloy anode materials in way that they can sustain high pressures.

3 Elasticity design of lithium metal anode

3.1 Transport and mechanical challenges for lithium metal

Li metal anode demonstrates a high specific capacity (3860 mAh g^{-1}) and volumetric capacity (2211 mAh cm^{-3}) [3,14,66]. However, unlike Li alloys, Li metal anode does not have a host, and the electrochemical reaction is entirely based on the Li electrodissolution and deposition. There is a tremendous push toward solid-state Li metal batteries which implement anode-free designs to maximize the cell-level energy density [67,68]. In an anode-free architecture, the active material resides in the host cathode. During electrodeposition, the lithium is plated directly on the current collector. The reversibility of solid-state Li metal anode is governed by a range of different mechanisms including chemo-mechanical failure of solid electrolyte, lithium filament/dendrite formation, delamination of Li from the solid electrolyte, etc [15,69–73].

Most of solid electrolytes are chemically unstable with Li metal, which requires an additional interlayer between solid electrolyte and lithium metal anode. Side reactions at Li|solid electrolyte interfaces can result in the formation of an interphase region [3,4,14]. If the interphase is electrically conducting it can grow uncontrollably and lead to large cell polarization. To overcome this challenge, there is a significant body of work focused on designing an interlayer or artificial solid electrolyte interphase between Li and solid electrolyte [74–78]. Of notice, the additional of interlayer dilutes the energy density of lithium metal. The highest specific capacity of the composite Li anode is 1000 mAh g^{-1}, which is only 1/4 of its theoretical capacity (Table 2).

To increase lifetime of a Li metal anode, it is also critical to achieve understand the dynamic process of Li dissolution/deposition. Lithium deposition involves heterogeneous Li nucleation and growth [79]. The solid electrolyte can be pushed outward during deposition and the lithium metal experiences compressive stresses. Regions with low compressive stress can lead to non-uniform ion flux and non-uniform plating [80]. These 'hot-spots' may initiate filament formation and short the cell [81].

To mitigate Li filaments or dendrites, it is important to homogenize the ion, electron and stress fields. According to nucleation and growth theory, during Li plating, the surface overpotential needs to overcome the nucleation energy barrier to trigger nucleation. Lithiophilic coating or materials with a low absorption energy barrier towards Li, can perform as the preferential nucleation sites [17] As shown in Table.2, different types of lithiophilic materials have been used for solid-state lithium metal anode. Materials that can alloy with Li (e.g. Ag, Sn, Si) and the corresponding metal oxide have been widely explored [82–84]. Both of the interlayer and lithiophilic coating can function to homogenize the ion/electron distribution at the in-plane direction, especially at the initial stage, when there is a uniform and intimate contact. However, during long-term cycling the interface can get irregular, which can lead to non-uniform stress distributions.

Control over solid electrolyte mechanical properties (e.g. strength, elasticity, adhesion, etc.) and their subsequent interaction with the lithium metal anode is critical. Solid electrolytes, either rigid or soft, could homogenize the stress field leading to effective dendrite suppression based on specific mechanisms. Control over the chemo-mechanical interactions between solid-electrolytes and lithium metal is necessary to suppress pore formation and mitigate dendirte formation. The following discussion will discuss the underlying mechanisms for dendrite suppression and chemo-mechanical challenges for rigid and soft solid electrolytes, respectively.

3.1.1 Challenges for the rigid solid electrolytes

Rigid solid electrolytes can impose a uniform stress on Li surface and facilitate Li creep ((Fig. 6a) [88]. Continuous interfacial contact is important for maintaining uniform Li plating. External factors, such as pressure and temperature, may be a pathways to controlling this contact. Li metal has a low yield strength of 0.7 MPa [89], and thus even a moderate stack pressure (1∼10 MPa) can enable uniform contact [90]. However, applying a high pressure will lead to higher compressive stress and require a higher driving force for Li deposition [91,92]. Furthermore, it has been shown that pressure can cause electrical shorting of a solid electrolyte even with an applied current or voltage. Since solid electrolytes surfaces are microstructurally diverse the presence of cracks, grains, and edges, which can cause irregular contact and Li can creep into these microstructural features under an applied pressure. High local compressive stress would lead to higher local plating rates and dendrite formation [66,93–95]. The Li dendrite stretches and shears specific spots on the solid electrolytes, resulting in the continuous growth of crack across the solid electrolyte and failure of the battery [96].

3.1.2 Challenges for the soft solid electrolytes

Soft solid electrolytes (e.g. sulfides, polymers, or hybrids) can achieve a good contact with Li metal under small stack pressures [97]. Sulfide solid electrolytes demonstrate Young's modulus around 30 GPa and polymer electrolytes range from 1 MPa to 1 GPa. With a higher elasticity, the soft solid electrolytes can withstand the large local volume expansion of Li metal (Fig. 6b). The stressed solid electrolyte imposes a compressive stress on the Li metal anode and prevents the formation of hot-spots [98]. While soft interfaces enable intimate contact with Li metal, they also can suffer from the Li stripping-induced contact loss [99]. As a result, during Li stripping, voids emerge on the Li surface, resulting in poor contacts and enlarged interfacial resistance [14,15,100]. Also, soft solid electrolytes with low stiffness can wrinkle on the Li metal surface and result in low cycle lifetimes [101].

3.2 Electrode design for the Li anode

Non-uniform stress distribution can lead to local lithium metal deposition and insufficient compressive stress can contribute non-uniform contact between the electrode and solid electrolyte. Design of functional electrodes that can regulate stress and contact is a major challenge [72,102]. Recently, a soft and elastic polydimethylsiloxane (PDMS) film was implemented behind the copper current collector to facilitate force dissipation (Fig. 7a). PDMS is highly elastic (Young's modulus 2.6 MPa, compressive strain 40%) and can adsorb stress during deposition and expand during stripping to facilitating continous contact [103 104]. However, once the compressive strain limitations of PDMS may inhibit the

Table 2 Performance of the reported all-solid-state Li metal anodes.

Ref.	Electrolyte	Modification	Areal mass mg cm^{-2}	Capacity mAh cm^{-2}	Current mA cm^{-2}	Cycle
Choi et al.[85]	$Li_{10}GeP_2S_{12}$	Graphite interlayer	8.677	0.5	0.2	100
Chen et al.[86]	LiPON	ZnO/CNT array	0.91	0.82	2.0	50
Xu et al.[87]	LLZTO	ZnO-porous LLZTO	14.6	6.3	0.27	50
Im et al.[17]	Li_6PS_5Cl	Ag/C interlayer	5.12	5.44	3.4	1000

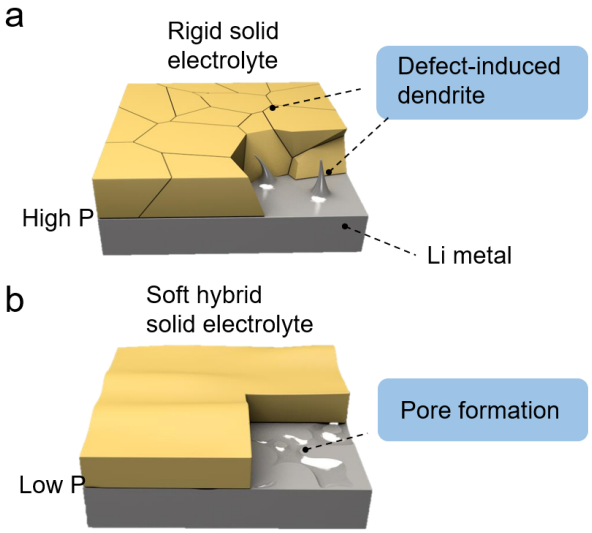

Fig. 6 Challenges facing the solid-state Li anode: Li|rigid solid electrolyte (a) and Li|soft solid electrolyte (b).

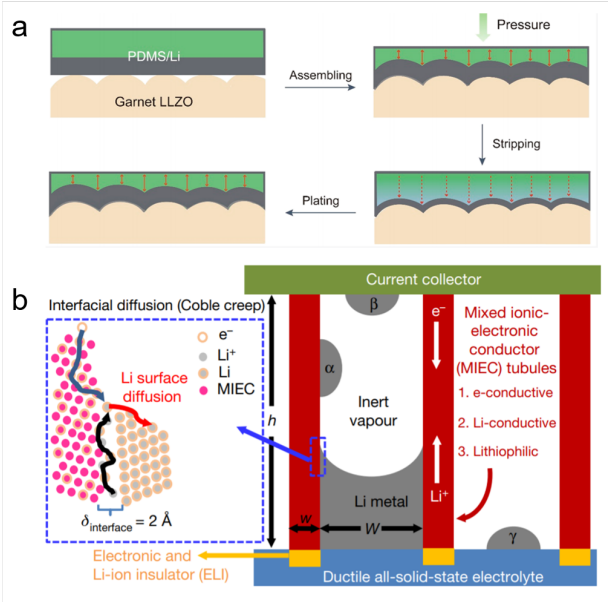

Fig. 7 Electrode design of Li metal anode. (a) Schematic illustration of the stress self-adapted interface by using compressible PDMS/Li metal anode. Reproduced with permission from[103] (Copyright 2020, American Chemical Society).(b) Schematic process of creep-enabled Li deposition/stripping in an MIEC tubular matrix, where Coble creep dominates via a interfacial diffusion along the MIEC/Li incoherent interface, Reproduced with permission from[86],(Copyright 2020, Nature Publishing Group).

use of pressure during operation. Another design approach used to alleviate stress build up in Li metal is architectures that facilitate Li creep flow (Fig. 7b). A recent study employed a mixed ion/electron conductive (MIEC) ZnO-coated carbon nanotube array as the current collector for Li metal[86]. This study discovered that single-crystal Li metal can grow out of and retract inside the tubules via diffusional Coble creep along the MIEC/Li phase boundary. Creep is the tendency of a solid material to move slowly or deform permanently under the influence of persistent mechanical stresses. At room temperature, the homologous temperature for Li is $T/T_M = 0.66$, so lithium metal can demonstrate noticable creep as a result of plating-induced stress. This strategy alleviates interfacial stress via removing excess lithium metal from the interface. However, this approach relies on ordered CNT arrays which will require a relatively soft solid electrolyte. The electrode design utilizing the MIEC interface has been demonstrated with solid-state batteries in an anode-free configuration[17]. Alloy interlayer (Ag) may be a pathway to stabilize Li plating/stripping at solid electrolyte interfaces under applie pressures (> 2 MPa). The alloy can facilitate uniform Li nucleation due to a low absorption energy barrier and effective transport to and from the current collector (stripping and plating). Ultimately, stress relief and uniform ionic fluxes are necessary to avoid the formation of filaments and catastraphic failure. Theoretically, both rigid or soft solid electrolyte could be selected as a solid electroltye for lithium metal if stress can be regulated.

4 Elasticity design for conversion cathode

4.1 Transport and mechanical challenges for the conversion cathode

Conversion type-cathodes (sulfur, FeF_2, etc.) are promising alternatives to layered oxides. Sulfur has a high gravimetric capacity and FeF_2 has a high volumetric capacity[105]. The conversion reaction can be described by:

$$S + 2Li^+ + 2e^- \rightarrow Li_2S \quad (4)$$

$$FeF_2 + 2Li^+ + 2e^- \rightarrow 2LiF + Fe \quad (5)$$

Several conversion cathodes suffer from low ion and electron transport properties[21] and large volumetric strains (80% for sulfur cathode, 30% for FeF_2 cathode). To achieve effective ion transport within the cathode, typically the active electrode material is combined with the solid electrolyte into a composite structure (Fig.8). The specific capacity, rate performance, and cycle lifetime is dependent on both the mechanical and transport prop-

erties of the cathode. These properties are largely dependent on the microstructure of the electrode which is governed by composition and meso-structural properties. Since, both S and Li_2S are insulating, the intermediate discharge product, Li_xS, can mediate Li^+ transport. But it is still insulating for electron. The low conductivity results in the relatively low fraction of active material (typically below 30 wt%) in the electrode as shown in Table 3. Sulfide solid electrolytes, such as Li_3PS_4 or Li_6PS_5Cl, can be incorporated with sulfur or Li_2S to improve the ionic conductivity[106–110]. Another approach is to create a composite cathode of S or Li_2S with mixed electronic and ionic conductors. Semiconductor sulfide compounds (TiS_2, FeS_2, P_2S_5, SeS_2, and etc) can improve electronic conductivity and facilitate surface or bulk Li diffusion. They can also store charge and thus can increase the cathode's capacity[111 112 113]. Pure sulfur or Li_2S usually need to be dispersed as nanoparticles (<10 nm) to increase bulk phase transport properties.

Sulfur cathodes can experience large volume changes that induce fracture of either the carbon and/or solid electrolyte matrix. Volume expansion can also lead to delamination and thus non-uniform ionic flux and capacity loss (Fig. 8). Macroscopic fracture in an all solid-state sulfur cathode was recently observed using transmission electron microscopy[114–116]. Increasing polarization during cycling is evidence of electrode fracture or delamination[115]. Cycling stability of solid-state sulfur cathodes are highly dependent on the depth of discharge (e.g. volume expansion)[114]. Recently, stable cycling was achieved when a cut-off voltage was set to 0.4∼3 V with an initial areal capacity around 2.6 mAh cm^{-2}[114]. However, when the initial areal capacity was raised to 3.6 mAh cm^{-2} (cut off voltage ∼3 V) rapid capacity decay was observed.

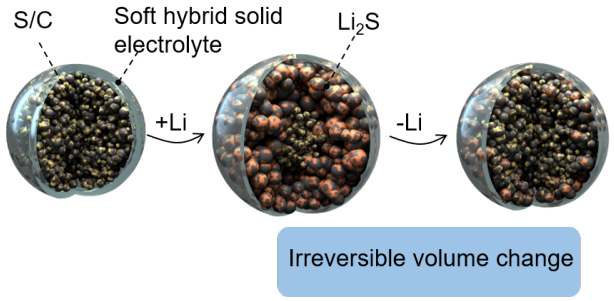

Fig. 8 Challenge facing the solid-state sulfur cathode.

Engineering cathodes with mechanically resilient microstructures is necessary for effective ion/electron transport and uniform contact. Beyond material's design strategies, there has been extensive work on operating conditions. Specifically, high external pressures have been employed to maintain uniform contact during cycling (volume expansion). Pressures exceeding 130 MPa (above the yield stress of the cathode) have been studied to mitigate the crack formation and maintain component contant[113,117,118]. These pressures are an order of magnitude higher than traditional batteries (<10 MPa)[91].

4.2 Electrode design for conversion cathode

Porous carbon materials are often employed as hosts for active sulfur. The carbon host needs to be well decorated to achieve effective Li^+ transport. However, there are trade-offs when considering transport and mechanical properties. A higher fraction of voids and smaller fraction of sulfur results in a better mechanical stability but poor transport. Thus, exquisite control over sulfur is necessary to balance these two competing entities. There are multiple different ways of incorporating sulfur in the carbon matrix, including but not limited to melt diffusion, vapor deposition, and solution infiltration. Carbon can also be coated with lithiated sulfur-based active material (e.g. Li_2S). It is challenging to infiltrate carbon with sulfur using melt diffusion or vapor deposition due to the limited wettability of molten or vapor sulfur on the carbon surface[120]. Alternatively, sulfur and CS_2 can be dissolved in the polar solvents. The selection of solvents can affect the interfacial energy between solution and carbon matrix. This greatly affects the sulfur distribution in the carbon matrix and electrochemical performance[121]. Another approach is to create a carbon matrix of coating directly on the sulfur. High temperature (usually 600 °C) treatment of Li_2S can induce graphitization. This approach leads to high carbon-sulfur contact.

Chemistry can also be exploited to create Li_2S/carbon composites. Lithium metal is known to spontaneously react with CS_2 to product Li_2S nanoparticles inside a graphitic carbon matrix (Li_2S@graphene). Theoretically, the mass fraction of Li_2S can reach as high as 90 % using this technique. Using this *in situ* reaction, leads to Li_2S particles wrapped in few-layered graphene (Fig. 9a)[116 122]. Precipitation and calcination of mixtures of Li_2S, Li_6PS_5Cl, and polyvinylpyrrolidone (PVP, carbon source) provided an effective strategy for achieving a mixed conductive composite (Fig. 9b)[106]. Lithiated active material (e.g. Li_2S) is unlikely to expand further and create damage to the carbon matrix.

During operation, a composite sulfur electrode requires the solid electrolyte to have an adequate elasticity (a lower Young's modulus and a larger elastic strain) to accommodate volume expansion and contraction. Operating trade-off will exist with regards to the cell overpotential and interfacial contact depending on the elasticity of the solid electrolyte. A highly elastic solid electrolyte will impose smaller stresses which will decrease the overpotential. However, interfacial ion transport may be limited. Assuming an 80% volume fraction of sulfur inside a spherical composite particle, the surrounding solid electrolyte needs to be stretched to 139% of its initial area. This is challenging for the inorganic solid electrolytes, but possible for the hybrid solid electrolyte.

Similar electrode and electrolyte design approaches can also apply to the FeF_2 cathode (Fig. 9c). FeF_2 can be incorporated into various types of porous carbon matrix using the scalable solution infiltration approaches[21,105,128]. A recent study achieved high cyclability of FeF_2 when combined with an elastic polymer (PEO) electrolyte (Fig. 9c)[119]. Highly elastic polymer electrolyte (induced by a higher EO:Li ratio (40:1)), can lead to a smaller overpotential, but a lower specific capacity (Fig.9c). This result

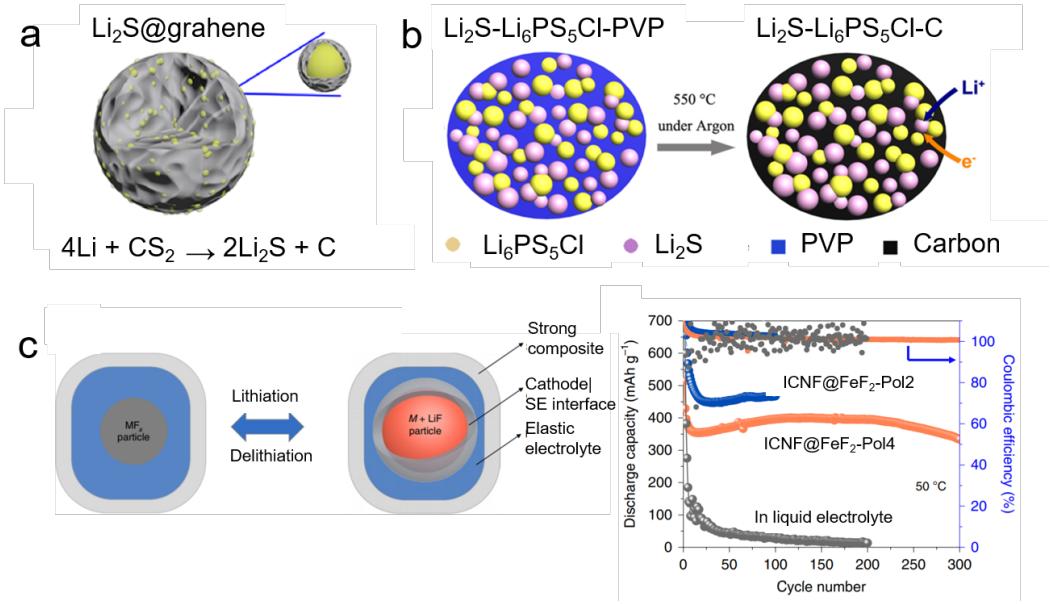

Fig. 9 Electrode design for sulfur cathode. (a) Schematic diagram of the Li_2S@C composite generated by the combustion of lithium metal with CS_2. Reproduced with permission from [116] (Copyright 2019, Nature Publishing Group). (b) Schematic diagram of Li_2S–Li_6PS_5Cl–C composite cathode fabrication based on a solution process. Reproduced with permission from [106] (Copyright 2018,American Chemical Society). (c) Schematic showing the the robust and flexible cathode electrolyte interface produced on the FeF_2 particle surface by using elastic SPE confined in a strong composite. Elastic CEI prevents continuous electrolyte decomposition and the problem of leaching of ions and substantially boosts cell-level stability.Reprinted with permission from [119] (Copy right 2019, Nature Publishing Group). Capacity of SPE-based FeF_2/CNF electrode (Pol2: EO:Li=20:1, Pol4:EO:Li=40:1) at 50 mA g^{-1} in comparison with the electrode cycled in liquid electrolyte at identical conditions. Reprinted with permission from [119] (Copy right 2019, Nature Publishing Group).

Table 3 Performance of the reported all-solid-state intercalation and conversion cathodes.

Ref.	Electrolyte	AM/carbon	AM loading mg cm^{-2}	Weight ratio	Capacity mAh cm^{-2}	Current mA cm^{-2}	Retention/ cycle number
Im et al. [17]	Li_6PS_5Cl	NMC/CNF	27.2	85%	5.44	3.4	90%/1000
Lin al. [123]	Li_2S-P_2S_5	S/MPC	0.6	30%	0.52	0.015	50%/300
Yao et al. [124]	Li_2S-P_2S_5	S/rGO	0.5	30%	0.42	0.75	88%/750
Han et al. [125]	$Li_7P_3S_{11}$	S/BP2000	0.6	30 %	0.6	3.0	0.98%/1200
Zhang et al. [126]	Li_2S-P_2S_5	S/CNT	1.1	30%	1.54	0.17	84%/500
Zhang et al. [127]	$Li_{10}GeP_2S_{12}$	$S_{0.95}Se_5$/pPAN	1.0	20%	1.35	0.17	77%/150
Xu et al. [115]	LiI-Li_2S-P_2S_5	Li_2S-LiI/VGCF	1.78	29%	2.3	0.32	33%/50
Yan et al. [20]	Li_2S-P_2S_5	Li_2S@graphene	7.0	38%	6.65	0.2	100%/30
Huang et al. [21]	PEO-LiTFSI	CNF@FeF_2	-	40%	-	0.1 C	58%/300

MPC: microporous carbon; rGO: reduced graphene oxide; pPAN: pyrolyzed polyacrylonitrile

highlights the dual roles elasticity might play on the high-strain electrodes. High elasticity makes the volume expansion easier, which decreases the overpotential. However, a high elasticity will reduce the stress imposed on the electrode, which slows down the ion transport and decreases the utilization ratio of active material. Hybrid electrolytes that combine an inorganic solid electrolyte with a polymer electrolyte may be a way to tailor both transport and cell overpotential in these composite systems

5 Design for rigid solid electrolyte

There are three main types of solid electrolytes being explored in solid-state batteries: oxide, sulfide, and polymer [129]. Inorganic solid electrolytes are typically more rigid than polymer type electrolytes. Oxide solid electrolytes include $Li_{1.3}Al_{0.3}Ti_{1.7}(PO_4)_3$, LiPON and the garnet-based Ta-, Ga-, Al-doped $Li_7La_3Zr_2O_{12}$ (LLZO) [130,131]. LLZO and LiPON exhibit reasonable ionic conductivities and high interface stability with Li metal. However, oxide solid electrolytes are usually mechanically brittle and require a high sintering temperature. There has been a significant effort to combine oxides (e..g garnets) with a polymer to achieve scalable processing [72,132–135]. In general, control over microstructure is challenging and largely governed by changes density controlled by processing [66,136].

Sulfide solid electrolyte include lithium thiophophate compounds like Li_3PS_4, $Li_7P_3S_{11}$, glassy Li_2S-P_2S_5 (LPS), argyrodite Li_6PS_5Cl and thio-LISICON-type $Li_{10}GeP_2S_{12}$ (LGPS). They stand out with their high ionic conductivity (10^{-3}-10^{-2} S cm^{-1}), high processability and low cost in terms of materials and synthesis. In addition, sulfide solid electrolyte is usually known as complaint compared with the oxide-based solid electrolyte (B/G>1.75, where B is the bulk modulus and G is the shear modulus in GPa). The Young's modulus of sulfide solid electrolytes range between

10-30 GPa, which is adequate for maintaining good interfacial contact with the electrode material. In addition to bulk mechanical properties, the solid electrolyte microstructure and processing conditions has also been shown to be important for load transfer [100].

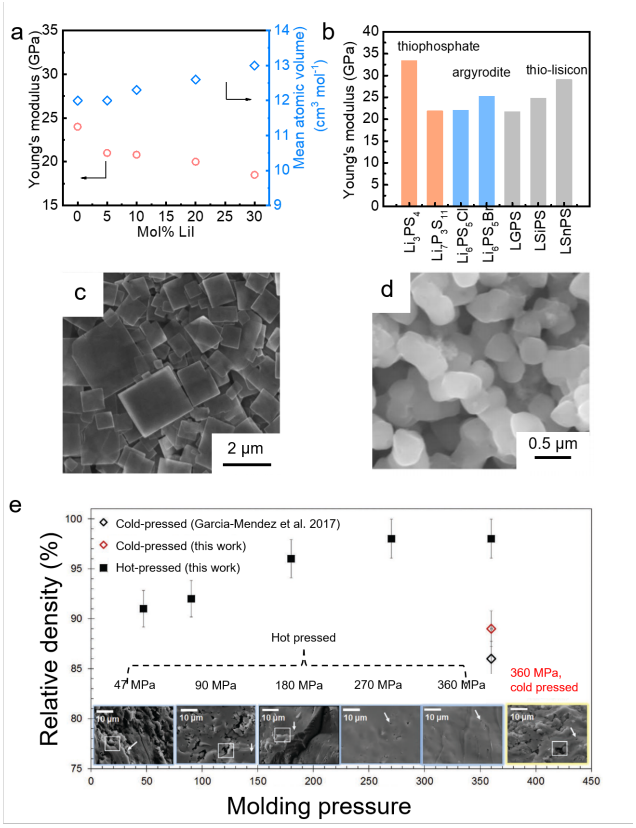

Fig. 10 Factors affecting the mechanical properties of sulfide solid electrolytes. (a) Young's modulus of glassy LPS as a function of LiI concentration. Reproduced with permission from [13]. (b) Young's modulus of sulfide solid electrolytes with different compositions [137]. (c) SEM image of plate-like, nanoscale building blocks of Li_3PS_4·2ACN. Reproduced with permission from [138](Copyright 2018, John Wiley and Sons Publisher). (d) SEM image of uniform Li_6PS_5Cl powder precipitate from the precursor solution containing 0.1 wt% surfactant. Reproduced with permission from [139] (Copyright 2018, Elsevier). (e) Relative density of glassy LPS75-25 as a function of molding pressure and temperature, the inset SEMs show the surface morphology of LPS under different molding conditions. Reproduced with permission from [140](Copyright 2020, John Wiley and Sons Publisher).

5.1 Structure-dependency

Microstructure heterogeneity can result in a range in mechanical properties in solid electrolytes. Glassy (amorphous) sulfide solid electrolytes demonstrate lower moduli when compared with glass-ceramics and crystalline sulfide solid electrolytes with similar compositions. Nanoidentation experiments reveal that the Young's modulus for dense Li_3PS_4 (E=20.3 GPa) is higher than Li_2S-P_2S_5 glass (E=18.5 GPa) [141 142]. The difference is attributed to the lack of periodic, long-range ordering and the presence of atomic free volume/dangling bonds. Recently, the addition of a halogen (LiI) to glassy LPS was shown to decrease the modulus (Fig. 10a). Halogen ions tend to increase the atomic free volume in the glass structure due to their relatively large size and high polarizability [13]. Generally, transport properties (ionic conductivity) increase with larger atomic free volume. Thus there might exist a trade-off between the transport (ionic conductivity) and mechanical (Young's modulus) properties. In addition to doping, cation and anion substitution can affect the Young's modulus. Experimental evaluation of mechanical properties has not yet been conducted for Si or Sn-substituted LGPS. However, computational investigations of Si- and Sn-substitution demonstrate an increase the modulus due to a greater ionic character of bonding (E=24.8 and 29.1 GPa, Fig. 10b) [137]. Anionic substitution of oxygen for sulfur may lead to enhanced mechanical properties [143].

5.2 Processing-dependency

Solid electrolyte processing conditions can impact mechanical properties. There are two primary processing routes explored in the literature: (1) mechanochemical and (2) solution-phase synthesis. Depending on the synthesis conditions a range of particle morphologies and sizes can be obtained. A disperesion of Li_3PS_4·3THF (THF is tetrahydrofuran) in acetonitrile (ACN) creates particles with nanoplate morphologies (Fig. 10c) [138]. Hot-pressing nanoplate sulfide solid electrolytes leads to the formation of free-standing Li_3PS_4 films with sub-micron thicknesses. Stacking nanoplates can maximize inner adhesion and minimize the solid electrolyte porosity. High adhesion and high density can lead to materials that can withstand high compressive forces. Particle morphology is heavily dependent of the working solvent or solution used during mechanochemical approaches [144]. While small particles can lead to denser pellets, it can also lead to more interfaces that dimish tranport properties. Thus, there is a delicate balance in terms of particle size and performance.

Li_6PS_5Cl can be prepared via mixing Li_3PS_4, LiCl and Li_2S in ethanol, followed by precipitation and sintering. Adding a surfactant (e.g. Titron 100) can diminish aggregation during the precipitation process [139]. Highly uniform size of 500 nm was obtained with a 0.1 wt% ratio of surfactant (Fig. 10d). A higher ratio of dispersant can further decrease the particle size, but the agglomeration effect becomes stronger, leading to a wider particle size distribution. Small solid electrolyte particle size in the cathode is helpful in enabling higher cathode material loading (e.g. 89 wt% $LiCoO_2$, 6 wt% Li_6PS_5Cl) at the expense of less percolation. Overall, small size, high-surface-area solid electrolyte powder is desirable for maintaining good interfacial contact and maintaining continuous ion-transport pathway across the electrode. However, the desirable particle size for the electrolyte in the cathode and bulk electrolyte may be different.

Processing temperature and pressure also impact electrolyte performance [145 146]. Previous studies systematically investigated the effect of temperature and pressure on the relative density (porosity), mechanical properties, transport properties, and composition (crystallinity) [147]. A high molding pressure of 180 MPa and a temperature of 200 °C can reduce porosity and particle boundaries while preserving the preferred amorphous structure for LPS75-25 [147] (Fig. 10e). The Young's moduli of a sulfide solid

electrolyte decreases when the processing temperature is greater than the glass transition point (200 °C). In addition, high pressures can lead to segregation of Li and S atoms. The shear and Young's moduli at high molding pressures of 180 MPa (G=11.8 GPa, E=30.9 GPa) are twice as high as their respective moduli at moderate pressures of 47 MPa (G=6.4 GPa, E=16.7 GPa). Processing material under pressure can impact structure and transport properties. The quantity of crystalline phases in LPS 75-25 increases as the temperature. Thio-LISICON III analog precipitate from the LPS glass at 170∼250 °C[140,146]. At a high pressing pressure (e.g.larger than 90 MPa), the lack of pores or free surfaces suppresses nucleation or growth of the crystalline or metastable crystalline phases. Exquisite control over processing temperature (200 °C) and pressure (180 MPa) can lead to dense, amorphous, and highly conducting glass LPS (1.1 mS cm^{-1} at room temperature).

Fracture toughness usually decreases with increasing part density and hot pressing[38]. It is difficult to handle a sulfide solid electrolyte derived from hot pressing at 360 MPa (200 °C). A modified hot pressing process, warm isostatic press,is more suitable for applying a uniform pressure on large-area solid electrolyte/electrode film[17]. The optimum pressure reached as high as 490 MPa using this technique. After pressing, the large-format, thin (50 μm in thickness) argyrodite Li_6PS_5Cl solid electrolyte sheet can be denser, more rigid while still maintains the freestanding property.

6 Design for soft solid electrolyte

Fabricating soft and elastic solid electrolytes requires combining an inorganic solid electrolyte material (e.g. sulfide) with a polymer binder[148]. Sulfide solid electrolytes enable ion transport and the polymer improves component elasticity. Electrolyte microstructure design needs to address solid electrolyte chemical stability with both processing solvents and polymer selection. Prior work investigated the role solvents and slurry composition impacts adhesion properties (Fig. 11a)[149]. Solvents with polarity index below 3.1 (blue region in Fig. 11a)) are fully compatible with sulfide solid electrolytes. Binders with a high polarity enable greater adhesion with sulfide-type solid electrolytes. Yet, high polarity polymer require polar solvents for dissolution. Non-polar binders, such as BR and NBR, can be dissolved in low-polarity solvents, but demonstrate limited adhesion. The trade-off could be reached by tuning the binder compositions. For instaince, polystyrene-block-polybutadiene-blockpolystyrene (SBS) rubber reacted with 3-mercaptocarboxylic acid can form a binder (C4 ∼ C40) with tailored adhesive and polar properties.

Solution based processing routes are ideal for achieving fast processing speeds. However, may solvents react with solid electrolyte materials. Sulfide solid electrolyte material e.g. $Li_7P_3S_{11}$) will change color when combined with most polar solvents (Fig. 11b)[150]. Raman spectroscopy detected a considerable fraction of insulating $Li_4P_2S_6$ when sulfide-type solid electrolyte material are dispersed in polar solvents such as acetonitrile and dimethyl carbonate (Fig. 11c)[151]. Solvent selection should avoid the co-dissolution of the active materials (e.g. electrode) and sulfide solid electrolytes. The addition of sulfur can exacerbate the dissolution of LPS in various types of polar solvents[107]. Furthermore it has been shown that Li_2S and Li_6PS_5Cl can co-dissolve in polar solvents such as ethanol[106].

Many polymers are incompatible with sulfide solid electrolytes. Polyethlyene oxide (PEO), polyvinylpyrrolidone (PVP), carboxymethyl cellulose (CMC) and PVDF are just a few examples of polymers that can decompose upon contact. Electron-rich atoms within the polymer backbone, including O, N and F, tend to form electrostatic interactions with the strong nucleophilic cations containing aliovalent atoms such as P or transition metals[152]. This can result in the localized sulfide solid electrolyte-polymer binder interaction that impede both ionic conductivity and adhesive properties of the polymer. Characterization of the interface between $Li_{10}SnP_2S_{12}$ (LSnPS) and dry-processed PEO_{15}:LiTFSI, showed the formation of polysulfide and sulfites. These observations were identified using a host of characterization techniques including XPS, ultraviolet-visible spectroscopy (UV-Vis) and 31P MAS NMR[153]. The decomposition reactions can lead to increased interface resistance, due to the formation of insulating product[154]. Prior results suggest that decomposition is driven by polymerization of thiophosphate units generating corner- and edge-sharing species, namely $Li_4P_2S_7$,$Li_2P_2S_6$[155,156](Fig. 12). This reaction can result in the reduction of Li-ion sites, sulfur release, and the formation of lithium polysulfides. Lithium polysulfides can be dissolved in PEO and drive decomposition and intramolecular fragmentation. Polymer fragmentation is accelerated by the deprotonation of PEO and LiOH impurity[157]. The resulting alkoxides can react with polysulfides to form sulfite and polymer fragments[158] (Fig. 12).

Two potential directions are being pursued for hybrid solid electrolytes processing: (1) dry-processing sulfide solid electrolyte with a self-healing polymer, and (2) slurry-processing sulfide solid electrolyte using stable polymer (monomer)/solvent. The first approach requires the combination of a malleable polymer (e.g polyimine) with a LPS powder via high-energy ball milling. After hot pressing, the thermoset polyimine polymer will be impregnated into the void space between LPS powder and create a continuous host for LPS, due to dynamic covalent bonding of reversible crosslinks within the network (Fig. 13a)[31]. This method is particularly useful for avoiding the use of a solvent. However, the preparation requires tedious mixing for dispersion and it is often challenging to control microstructure and polymer arrangement which can affect transport properties. Furthermore, chemically compatibility with self-healing polymers is unknown. Alternatively, sulfide solid electrolytes can processed in a solution form if combined with polymers with low or no electronegative functional groups and non-polar solvents (Fig. 12)[150]. A potential consequence of using a polymer with limited electronetative functional groups is poor adhesion. Given these trade-offs, there is growing interest in exploring the sulfide solid electrolyte-catalyzed polymerization to improve interfacial adhesion[159,160]. Most of sulfide units exhibit nucleophilicity and catalytic activity that can promote the polymerization reaction. Li_3PS_{4+x} (x=1.5), as the solid electrolyte performs a catalytic role to initiate the ring opening polymerization of liquid ethylene sulfide (ES) precursor, embedding nanosized Li_3PS_{4+x} inside the elastic polyethylenesul-

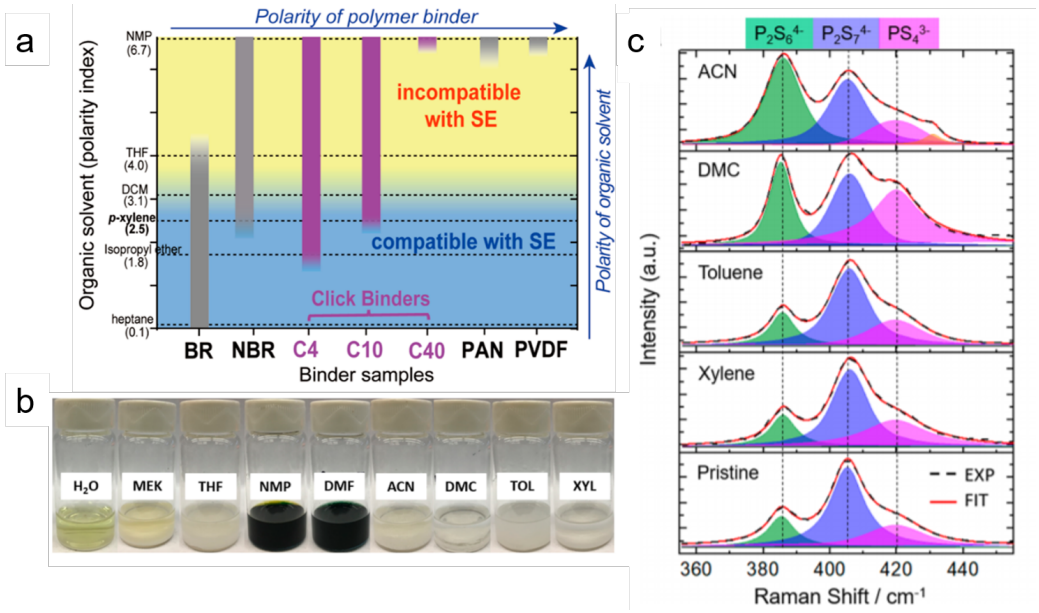

Fig. 11 Challenges of fabricating sulfide solid electrolyte/polymer hybrid electrolyte. (a) Solubilities of various binders in solvents with different polarities. Compatibility of the solid electrolyte with solvents is indicated in blue (compatible) and yellow (incompatible) regions. Reproduced with permission from [149](Copyright 2018, American Chemical Society). (b) Different solvent color changes after addition of $Li_7P_3S_{11}$. (c) Deconvoluted Raman spectra of $Li_7P_3S_{11}$ after dispersion in different solvents Reproduced with permission from [150](Copyright 2019, American Chemical Society).

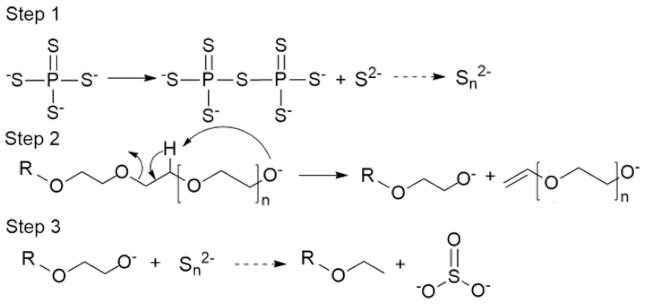

Fig. 12 Decomposition of sulfide solid electrolyte induced by polymer electrolytes [156](Copyright 2015, Electrochemical Society).

fide matrix (Fig. 13b) [159].

In addition, sulfide solid electrolytes can chemically crosslink with polymers to create covalent bonding. Crosslinking between LPS and PFPE-diol polymer can occur via a spontaneous reaction between LPS and hydroxyl groups on PFPE [160,161].It was shown that with 23 wt% polymer, the shear modulus (G) of the hybrid electrolyte can be reduced to 2.6 MPa which is approximately three orders of magnitude lower than that of LPS (around 8 GPa for LPS). This decrease in shear moduli is accompanied with increase in elasticity. PFPE-diol polymer with a high fluorine content does not solvate the lithium polysulfides which leads to lower decomposition (Fig. 13). Furthermore, the formation of covalent bonds between the polymer and inorganic phase potentially is favorable for long-term stability of sulfide solid elctrolyte.

7 Characterization approaches

Advanced characterization combined with theory are necessary to understand the mechanical properties of hybrid, polymer, and all-inorganic solid electrolytes. These systems are particularly challenging to probe because material transformation and evolution occurs and buried solid-solid interfaces. Thus, detection approaches are typically limited by temporal or spatial resolution. Thus, to effectively evaluate these material systems requires static and dynamic testing approaches.

7.1 Static characterization

Young's modulus is a characteristic mechanical property which describes the tensile and compressive stiffness of a material. It is also often a descriptor used to describe elasticity. Experimentally Young's moduli can be estimated using nanoindentation approaches, acoustic methods, or traditional mechanical testing. The latter however is limited to macros-scale measurements. Nanoidentation typically is performed at a single particle or grain and thus reflects the intrinsic mechanical properties of material [147,162]. Acoustic measurements are non-destructive and displaces particles via propagation of a longitudinal or shear wave which enables measurement of large-area (1 cm^2) elastic properties [142]. Solid electrolyte microstructure heterogenities (e.g. grain boundary, voids, etc.) have a significant impact on mechanical properties and stress distribution. Electrochemical strain microscopy (ESM) with atomic force microscopy has been used to examine impact of nano-scale irregularities. Under an external voltage bias, the techniques can examine the variations of strain led by difference of Li concentration [72,73,100,163–167]. Yet, the challenge with *in situ* microscopy cells is that a surface needs to be exposed, and thus maintaining uniform pressure is challenging.

Fracture toughness is a measure of the total force or stress a material can experience before catastrophic failure [168,169].

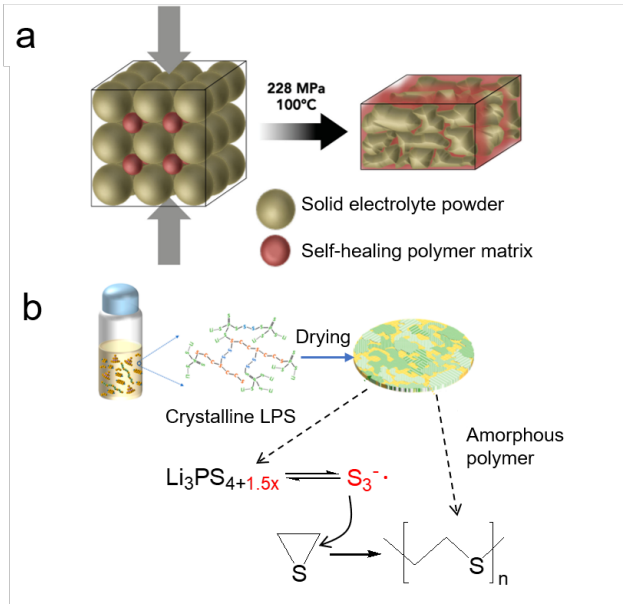

Fig. 13 Approaches of hybrid sulfide solid electrolytes with polymers. (a) Schematic showing the pellet pressing process using self healing polymer as the binder for LPS. Reproduced with permission from [31] (Copyright 2015, John Wiley and Sons Publisher). (b) Schematic images for Li_3PS_{4+x}/PES synthesis and its structure. Reproduced with permission from [159] (Copyright 2020, American Chemical Society).

Nanoindentation can measure the fracture toughness at a small scale. Nanoindention works via inducing local stress distribution upon loading and penetration [170]. The stress-strain curve under different stretching rates may be required to estimate properties and reflects the electrolyte's capability to withstand the large volume change under different current densities [171].

7.2 Dynamic Characterization

Static characterization is valuable for evaluating local properties at equilibrium. However, there is also interest in understanding how material properties change at non-equilibrium or dynamic states during electrochemical cycling [14,15,66,175]. Atomic force microscopy can be combined with *in situ* environmental transmission electron microscope to visualize the volume/composition change under a controllable elastic constraint, and an external voltage bias (Fig. 14a) [172]. For example, the AFM–ETEM set-up can directly visualize the Li filament growth driven by a high local stress, and evaluate the mechanical behavior of the Li filament under different elastic constraints (Fig. 14b). This characterization approach has also be implemented on electrode materials under an elastic constraint (e.g. Sulfur, Silicon, etc.) [116]. The major drawback of this approach is in the sample geometry. Only a small fraction of the electrode can be probed and is connected to the solid electrolyte. This requires the electrode material to be intrinsically ionically-conductive. Similarly, AFM cantilever can be integrated into the scanning electron microscope to visualize the strain of microsized electrode particles [176].

In addition to electron microscopy, X-ray characterizations can study the electrode particle's behavior. Coherent X-ray diffraction imaging (CDXI) can construct the 3D electron density mapping and atomic displacement fields in materials through the interference produced by coherent X-rays and phase-retrieval algorithms [177]. Therefore, CDXI can study the strain evolution, electron density distribution, and lattice distortions under operando conditions.

X-ray computed tomography characterization can capture the morphology change in the three-dimensional domain (Fig. 14c,d) [14,15,66,73,178 174]. Phase contrast provided by a synchrotron X-ray source can further detect the differences for the individual materials (including active materials, carbon, solid electrolyte and polymer) within the electrode [179]. Therefore, the volume change of electrode materials could be correlated with the (de)lithiation state. The X-ray CT data can be further analyzed by the digital image correlation (DIC) techniques to analyze the strain distribution [180 181]. In order to analyze the large quantity of data in the three-dimensional domain, recent study demonstrates the application of machine learning algorithm on the statistical analysis the material damage. The combination of X-ray tomagraphy and advanced numerical tool would be particularly useful for analyzing the coupled chemo-mechanical phenomena inside solid-state battery electrodes.

8 Discussion and future outlook

Overall, design of solid-state batteries and understanding how they operate is still in the early stage of development. The rational design requires a coalescence of electrochemistry, mass transport, mechanics and material science. There are many open questions that need to be explored for rapid adoption of high performing solid state batteries. Solid state batteries represent a very promising pathway toward the integration of energy dense anode. Yet, exquisite control over chemo-mechanics is going to be necessary for long term cycling of either lithium metal and/or silicon anodes. In addition, to the anode, there is little known about the composition and make up of solid state cathodes. The carbon-binder domain is especially important for maintaining the structural stability of solid-state cathodes and anodes. Emerging materials that can replace carbon, such as transition metal carbide, can provide superior mechanical, transport and chemical properties. Also the selection of binder remains largely unexplored in this field. Finally, most solid-state batteries are still fabricated and tested at lab scale . Roll-to-roll manufacturing processes with similar scales and speeds at traditional batteries are necessary for adoption of solid state batteries in electric vehicle applications. Future manufacturing approaches will ultimately need to be able to control interfaces (electrode/electrolyte) and microstructure (density). Current calendaring processes may need to be modified depending on the materials selected.

Conflicts of interest

The authors declare no financial interest.

Acknowledgements

The authors were supported by the National Science Foundation under grant No. 1847029.

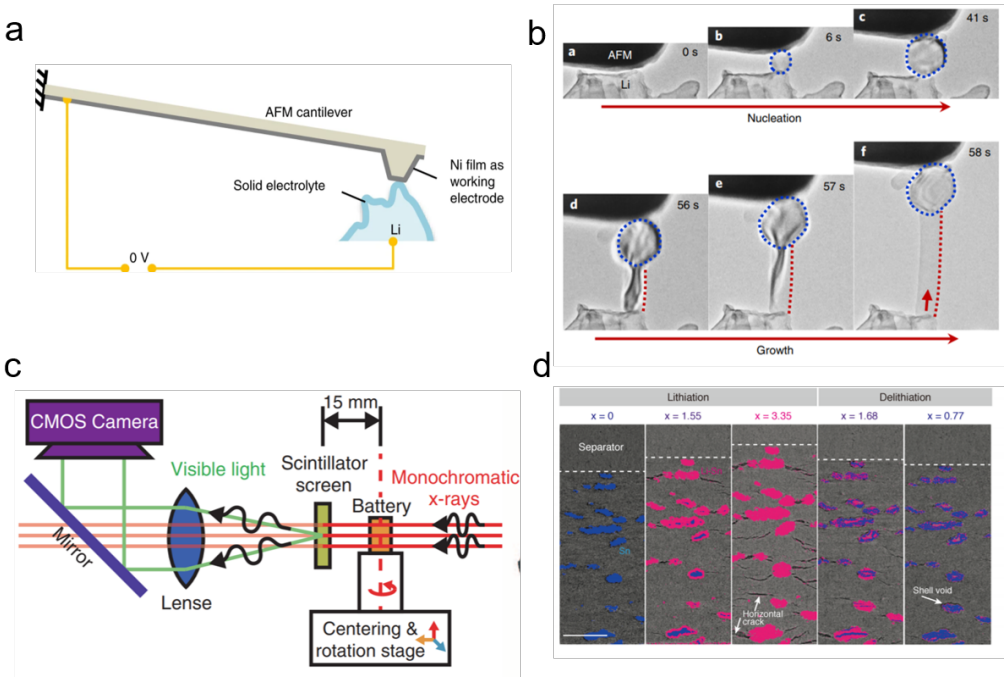

Fig. 14 Measurement of the interfacial stress/strain evolution. (a) Schematic of AFM/ETEM for in situ study. (b) TEM snapshots of Li particle nucleation and filament growth process. Reproduced with permission from [172] (Copyright 2020, Nature Publishing Group). (c) Schematic of X-ray CT for in situ study. Reproduced from permission [173] (Copyright 2013, AAAS). (d) Cross sectional CT image of solid-state electrode fabricated from LPS and Li_xSn at various depths of lithiation (x is the number of Li in Li_xSn). The Sn and Li_xSn phases are coloured in blue and pink, respectively. Reproduced with permission from [174] (Copyright 2019, John Wiley and Sons Publisher).

References

1 F. Wu, J. Maier and Y. Yu, *Chemical Society Reviews*, 2020, **49**, 1569–1614.

2 B. Dunn, H. Kamath and J.-M. Tarascon, *Science*, 2011, **334**, 928–935.

3 K. B. Hatzell, X. C. Chen, C. Cobb, N. P. Dasgupta, M. B. Dixit, L. E. Marbella, M. T. McDowell, P. Mukherjee, A. Verma, V. Viswanathan *et al.*, *ACS Energy Letters*, 2020.

4 K. B. Hatzell, *Joule*, 2020, **4**, 719–721.

5 Q. Zhang, D. Cao, Y. Ma, A. Natan, P. Aurora and H. Zhu, 2019, **1901131**, 1–42.

6 R. Chen, Q. Li, X. Yu, L. Chen and H. Li, *Chemical Reviews*, 2019.

7 Y. Liu, G. Zhou, K. Liu and Y. Cui, *Accounts of chemical research*, 2017, **50**, 2895–2905.

8 F. J. Simon, M. Hanauer, F. H. Richter and J. Janek, *ACS Applied Materials and Interfaces*, 2020, **12**, 11713–11723.

9 F. Wu, J. Maier and Y. Yu, *Chemical Society Reviews*, 2020, **49**, 1569–1614.

10 S. Zhang, *npj Computational Materials*, 2017, **3**, 1–10.

11 P. Wang, W. Qu, W. L. Song, H. Chen, R. Chen and D. Fang, *Advanced Functional Materials*, 2019, **29**, 1–29.

12 F. Zhang, Q. A. Huang, Z. Tang, A. Li, Q. Shao, L. Zhang, X. Li and J. Zhang, *Nano Energy*, 2020, **70**, 104545.

13 A. Kato, M. Yamamoto, A. Sakuda, A. Hayashi and M. Tatsumisago, *ACS Applied Energy Materials*, 2018, **1**, 1002–1007.

14 M. B. Dixit, N. Singh, J. P. Horwath, P. D. Shevchenko, M. Jones, E. A. Stach, T. S. Arthur and K. B. Hatzell, *Matter*, 2020.

15 M. B. Dixit, A. Verma, W. Zaman, X. Zhong, P. Kenesei, J. S. Park, J. Almer, P. P. Mukherjee and K. B. Hatzell, *ACS Applied Energy Materials*, 2020, **3**, 9534–9542.

16 D. Hyeon, H. Ah, Y. Bae, J. Woo, S.-m. Lee and Y. Seok, *Journal of Power Sources*, 2019, **426**, 143–150.

17 Y. G. Lee, S. Fujiki, C. Jung, N. Suzuki, N. Yashiro, R. Omoda, D. S. Ko, T. Shiratsuchi, T. Sugimoto, S. Ryu, J. H. Ku, T. Watanabe, Y. Park, Y. Aihara, D. Im and I. T. Han, *Nature Energy*, 2020.

18 Y. J. Nam, D. Y. Oh, S. H. Jung and Y. S. Jung, *Journal of Power Sources*, 2018, **375**, 93–101.

19 M. A. Kraft, S. Ohno, T. Zinkevich, R. Koerver, S. P. Culver, T. Fuchs, A. Senyshyn, S. Indris, B. J. Morgan and W. G. Zeier, *Journal of the American Chemical Society*, 2018, **140**, 16330–16339.

20 H. Yan, H. Wang, D. Wang, X. Li, Z. Gong and Y. Yang, *Nano letters*, 2019, **19**, 3280–3287.

21 Q. Huang, T. P. Pollard, X. Ren, D. Kim, A. Magasinski, O. Borodin and G. Yushin, *Small*, 2019, **15**, 1804670.

22 A. Mistry and P. P. Mukherjee, *Journal of The Electrochemical Society*, 2020, **167**, 082510.

23 H. Wu, G. Chan, J. W. Choi, I. Ryu, Y. Yao, M. T. McDowell, S. W. Lee, A. Jackson, Y. Yang, L. Hu *et al.*, *Nature nanotechnology*, 2012, **7**, 310–315.

24 E. Pollak, G. Salitra, V. Baranchugov and D. Aurbach, *The*

Journal of Physical Chemistry C, 2007, **111**, 11437–11444.
25 N. Ding, J. Xu, Y. Yao, G. Wegner, X. Fang, C. Chen and I. Lieberwirth, *Solid State Ionics*, 2009, **180**, 222–225.
26 N. Nitta and G. Yushin, *Particle & Particle Systems Characterization*, 2014, **31**, 317–336.
27 M. D. Levi and D. Aurbach, *The Journal of Physical Chemistry B*, 1997, **101**, 4641–4647.
28 J. Chen, X. Fan, Q. Li, H. Yang, M. R. Khoshi, Y. Xu, S. Hwang, L. Chen, X. Ji, C. Yang *et al.*, *Nature Energy*, 2020, 1–12.
29 S. Ito, S. Fujiki, T. Yamada, Y. Aihara, Y. Park, T. Y. Kim, S.-W. Baek, J.-M. Lee, S. Doo and N. Machida, *Journal of Power Sources*, 2014, **248**, 943–950.
30 J. M. Whiteley, J. W. Kim, D. M. Piper and S.-H. Lee, *Journal of The Electrochemical Society*, 2015, **163**, A251.
31 J. M. Whiteley, P. Taynton, W. Zhang and S. H. Lee, *Advanced Materials*, 2015, **27**, 6922–6927.
32 A. F. Bower, P. R. Guduru and V. A. Sethuraman, *Journal of the Mechanics and Physics of Solids*, 2011, **59**, 804–828.
33 J. Cannarella, C. Z. Leng and C. B. Arnold, Energy Harvesting and Storage: Materials, Devices, and Applications V, 2014, p. 91150K.
34 G. Bucci, T. Swamy, S. Bishop, B. W. Sheldon, Y.-M. Chiang and W. C. Carter, *Journal of The Electrochemical Society*, 2017, **164**, A645–A654.
35 L. A. Berla, S. W. Lee, Y. Cui and W. D. Nix, *Journal of Power Sources*, 2015, **273**, 41–51.
36 G. Bucci, T. Swamy, Y.-M. Chiang and W. C. Carter, *Journal of Materials Chemistry A*, 2017, **5**, 19422–19430.
37 J. A. Lewis, J. Tippens, F. J. Q. Cortes and M. T. McDowell, *Trends in Chemistry*, 2019, **1**, 845–857.
38 Y. Zhao, P. Stein, Y. Bai, M. Al-Siraj, Y. Yang and B.-X. Xu, *Journal of Power Sources*, 2019, **413**, 259–283.
39 X. H. Liu, L. Zhong, S. Huang, S. X. Mao, T. Zhu and J. Y. Huang, *ACS nano*, 2012, **6**, 1522–1531.
40 K. Zhao, M. Pharr, Q. Wan, W. L. Wang, E. Kaxiras, J. J. Vlassak and Z. Suo, *Journal of The Electrochemical Society*, 2011, **159**, A238.
41 X. Xu, J. Cheng, Y. Li, X. Nie, L. Dai and L. Ci, *Journal of Solid State Electrochemistry*, 2019, **23**, 3145–3151.
42 D. Y. Oh, D. H. Kim, S. H. Jung, J. G. Han, N. S. Choi and Y. S. Jung, *Journal of Materials Chemistry A*, 2017, **5**, 20771–20779.
43 X. H. Liu, L. Zhong, S. Huang, S. X. Mao, T. Zhu and J. Y. Huang, *ACS nano*, 2012, **6**, 1522–1531.
44 Z. Jiang, J. Li, Y. Yang, L. Mu, C. Wei, X. Yu, P. Pianetta, K. Zhao, P. Cloetens, F. Lin *et al.*, *Nature communications*, 2020, **11**, 1–9.
45 S. W. Lee, M. T. McDowell, L. A. Berla, W. D. Nix and Y. Cui, *Proceedings of the National Academy of Sciences*, 2012, **109**, 4080–4085.
46 K. Zhao, W. L. Wang, J. Gregoire, M. Pharr, Z. Suo, J. J. Vlassak and E. Kaxiras, *Nano letters*, 2011, **11**, 2962–2967.
47 Y. Jin, B. Zhu, Z. Lu, N. Liu and J. Zhu, *Advanced Energy Materials*, 2017, **7**, 1700715.
48 J. M. Whiteley, J. W. Kim, C. S. Kang, J. S. Cho, K. H. Oh and S.-H. Lee, *Journal of The Electrochemical Society*, 2015, **162**, A711–A715.
49 N. Ohta, S. Kimura, J. Sakabe, K. Mitsuishi, T. Ohnishi and K. Takada, *ACS Applied Energy Materials*, 2019, **2**, 7005–7008.
50 D. Lin, Z. Lu, P.-C. Hsu, H. R. Lee, N. Liu, J. Zhao, H. Wang, C. Liu and Y. Cui, *Energy & Environmental Science*, 2015, **8**, 2371–2376.
51 X. Zuo, J. Zhu, P. Müller-Buschbaum and Y.-J. Cheng, *Nano Energy*, 2017, **31**, 113–143.
52 M.-H. Park, M. G. Kim, J. Joo, K. Kim, J. Kim, S. Ahn, Y. Cui and J. Cho, *Nano letters*, 2009, **9**, 3844–3847.
53 L. Zhang, C. Wang, Y. Dou, N. Cheng, D. Cui, Y. Du, P. Liu, M. Al-Mamun, S. Zhang and H. Zhao, *Angewandte Chemie International Edition*, 2019, **58**, 8824–8828.
54 Y. Jin, B. Zhu, Z. Lu, N. Liu and J. Zhu, *Advanced Energy Materials*, 2017, **7**, 1700715.
55 K. Zhao, M. Pharr, L. Hartle, J. J. Vlassak and Z. Suo, *Journal of Power Sources*, 2012, **218**, 6–14.
56 C. A. Fernandez, N. M. Hortance, Y.-H. Liu, J. Lim, K. B. Hatzell and M. C. Hatzell, *Journal of Materials Chemistry A*, 2020, **8**, 15591–15606.
57 Y. Zhao, K. Zheng and X. Sun, *Joule*, 2018, **2**, 2583–2604.
58 F. Shen, M. B. Dixit, W. Zaman, N. Hortance, B. Rogers and K. B. Hatzell, *Journal of The Electrochemical Society*, 2019, **166**, A3182.
59 S. Cangaz, F. Hippauf, F. S. Reuter, S. Doerfler, T. Abendroth, H. Althues and S. Kaskel, *Advanced Energy Materials*, 2020, **10**, 2001320.
60 W. Ping, C. Yang, Y. Bao, C. Wang, H. Xie, E. Hitz, J. Cheng, T. Li and L. Hu, *Energy Storage Materials*, 2019, **21**, 246–252.
61 J. Sakabe, N. Ohta, T. Ohnishi, K. Mitsuishi and K. Takada, *Communications Chemistry*, 2018, **1**, 1–9.
62 J. Wang, L. Liao, Y. Li, J. Zhao, F. Shi, K. Yan, A. Pei, G. Chen, G. Li, Z. Lu *et al.*, *Nano letters*, 2018, **18**, 7060–7065.
63 Y. Son, N. Kim, T. Lee, Y. Lee, J. Ma, S. Chae, J. Sung, H. Cha, Y. Yoo and J. Cho, *Advanced Materials*, 2020, **32**, 2003286.
64 H. Jia, X. Li, J. Song, X. Zhang, L. Luo, Y. He, B. Li, Y. Cai, S. Hu, X. Xiao *et al.*, *Nature communications*, 2020, **11**, 1–9.
65 H. Wang, J. Fu, C. Wang, J. Wang, A. Yang, C. Li, Q. Sun, Y. Cui and H. Li, *Energy & Environmental Science*, 2020, **13**, 848–858.
66 M. B. Dixit, M. Regala, F. Shen, X. Xiao and K. B. Hatzell, *ACS applied materials & interfaces*, 2018, **11**, 2022–2030.
67 M. J. Wang, E. Carmona, A. Gupta, P. Albertus and J. Sakamoto, *Nature communications*, 2020, **11**, 1–9.
68 T. A. Zegeye, W.-N. Su, F. W. Fenta, T. S. Zeleke, S.-K. Jiang and B. J. Hwang, *ACS Applied Energy Materials*, 2020.
69 T. Krauskopf, F. H. Richter, W. G. Zeier and J. Janek, *Chemical Reviews*, 2020, **120**, 7745–7794.
70 P. Shi, X.-Q. Zhang, X. Shen, R. Zhang, H. Liu and Q. Zhang,

Advanced Materials Technologies, 2020, **5**, 1900806.
71 Y. Zhang, T.-T. Zuo, J. Popovic, K. Lim, Y.-X. Yin, J. Maier and Y.-G. Guo, *Materials Today*, 2020, **33**, 56–74.
72 M. B. Dixit, W. Zaman, Y. Bootwala, Y. Zheng, M. C. Hatzell and K. B. Hatzell, *ACS applied materials & interfaces*, 2019, **11**, 45087–45097.
73 M. B. Dixit, D. Moreno, X. Xiao, M. C. Hatzell and K. B. Hatzell, *ACS Materials Letters*, 2019, **1**, 71–76.
74 Y. Su, L. Ye, W. Fitzhugh, Y. Wang, E. Gil-González, I. Kim and X. Li, *Energy & Environmental Science*, 2020, **13**, 908–916.
75 Y. Mo, S. P. Ong and G. Ceder, *Chemistry of Materials*, 2012, **24**, 15–17.
76 L. Sang, K. L. Bassett, F. C. Castro, M. J. Young, L. Chen, R. T. Haasch, J. W. Elam, V. P. Dravid, R. G. Nuzzo and A. A. Gewirth, *Chemistry of Materials*, 2018, **30**, 8747–8756.
77 X. Yao, N. Huang, F. Han, Q. Zhang, H. Wan, J. P. Mwizerwa, C. Wang and X. Xu, *Advanced Energy Materials*, 2017, **7**, 1602923.
78 Y. Gao, D. Wang, Y. C. Li, Z. Yu, T. E. Mallouk and D. Wang, *Angewandte Chemie International Edition*, 2018, **57**, 13608–13612.
79 E. Kazyak, R. Garcia-Mendez, W. S. LePage, A. Sharafi, A. L. Davis, A. J. Sanchez, K.-H. Chen, C. Haslam, J. Sakamoto and N. P. Dasgupta, *Matter*, 2020.
80 L. Porz, T. Swamy, B. W. Sheldon, D. Rettenwander, T. Frömling, H. L. Thaman, S. Berendts, R. Uecker, W. C. Carter and Y.-M. Chiang, *Advanced Energy Materials*, 2017, **7**, 1701003.
81 L. Porz, T. Swamy, B. W. Sheldon, D. Rettenwander, T. Frömling, H. L. Thaman, S. Berendts, R. Uecker, W. C. Carter and Y.-M. Chiang, *Advanced Energy Materials*, 2017, **7**, 1701003.
82 M. Cai, Y. Lu, J. Su, Y. Ruan, C. Chen, B. V. Chowdari and Z. Wen, *ACS applied materials & interfaces*, 2019, **11**, 35030–35038.
83 K. K. Fu, Y. Gong, B. Liu, Y. Zhu, S. Xu, Y. Yao, W. Luo, C. Wang, S. D. Lacey, J. Dai *et al.*, *Science Advances*, 2017, **3**, e1601659.
84 B. Liu, L. Zhang, S. Xu, D. W. McOwen, Y. Gong, C. Yang, G. R. Pastel, H. Xie, K. Fu, J. Dai *et al.*, *Energy Storage Materials*, 2018, **14**, 376–382.
85 S.-J. Choi, S.-H. Choi, A. D. Bui, Y.-J. Lee, S.-M. Lee, H.-C. Shin and Y.-C. Ha, *ACS applied materials & interfaces*, 2018, **10**, 31404–31412.
86 Y. Chen, Z. Wang, X. Li, X. Yao, C. Wang, Y. Li, W. Xue, D. Yu, S. Y. Kim, F. Yang *et al.*, *Nature*, 2020, **578**, 251–255.
87 S. Xu, D. W. McOwen, L. Zhang, G. T. Hitz, C. Wang, Z. Ma, C. Chen, W. Luo, J. Dai, Y. Kuang *et al.*, *Energy Storage Materials*, 2018, **15**, 458–464.
88 M. J. Wang, R. Choudhury and J. Sakamoto, *Joule*, 2019, **3**, 2165–2178.
89 A. Masias, N. Felten, R. Garcia-Mendez, J. Wolfenstine and J. Sakamoto, *Journal of materials science*, 2019, **54**, 2585–2600.
90 J. Kasemchainan, S. Zekoll, D. Spencer Jolly, Z. Ning, G. O. Hartley, J. Marrow and P. G. Bruce, *Nat. Mater*, 2019, **18**, 1105–1111.
91 J.-M. Doux, H. Nguyen, D. H. Tan, A. Banerjee, X. Wang, E. A. Wu, C. Jo, H. Yang and Y. S. Meng, *Advanced Energy Materials*, 2020, **10**, 1903253.
92 J.-M. Doux, Y. Yang, D. H. Tan, H. Nguyen, E. A. Wu, X. Wang, A. Banerjee and Y. S. Meng, *Journal of Materials Chemistry A*, 2020, **8**, 5049–5055.
93 L. Porz, T. Swamy, B. W. Sheldon, D. Rettenwander, T. Frömling, H. L. Thaman, S. Berendts, R. Uecker, W. C. Carter and Y.-M. Chiang, *Advanced Energy Materials*, 2017, **7**, 1701003.
94 F. Shen, M. B. Dixit, X. Xiao and K. B. Hatzell, *ACS Energy Letters*, 2018, **3**, 1056–1061.
95 E. Kazyak, R. Garcia-Mendez, W. S. LePage, A. Sharafi, A. L. Davis, A. J. Sanchez, K.-H. Chen, C. Haslam, J. Sakamoto and N. P. Dasgupta, *Matter*, 2020.
96 C. E. Athanasiou, M. Y. Jin, C. Ramirez, N. P. Padture and B. W. Sheldon, *Matter*, 2020, **3**, 212–229.
97 M. B. Dixit, W. Zaman, N. Hortance, S. Vujic, B. Harkey, F. Shen, W. Y. Tsai, V. De Andrade, X. C. Chen, N. Balke and K. B. Hatzell, *Joule*, 2020, **4**, 207–221.
98 M. D. Tikekar, L. A. Archer and D. L. Koch, *Science advances*, 2016, **2**, e1600320.
99 J. Kasemchainan, S. Zekoll, D. Spencer Jolly, Z. Ning, G. O. Hartley, J. Marrow and P. G. Bruce, *Nat. Mater*, 2019, **18**, 1105–1111.
100 M. B. Dixit, W. Zaman, N. Hortance, S. Vujic, B. Harkey, F. Shen, W. Y. Tsai, V. De Andrade, X. C. Chen, N. Balke and K. B. Hatzell, *Joule*, 2020, **4**, 207–221.
101 Y. Liu, K. Guo, C. Wang and H. Gao, *Journal of the Mechanics and Physics of Solids*, 2019, **123**, 103–118.
102 W. Zaman, N. Hortance, M. B. Dixit, V. De Andrade and K. B. Hatzell, *Journal of Materials Chemistry A*, 2019, **7**, 23914–23921.
103 X. Zhang, Q. Xiang, S. Tang, A. Wang, X. Liu and J. Luo, *Nano Letters*, 2020, **20**, 2871–2878.
104 X. Wang, W. Zeng, L. Hong, W. Xu, H. Yang, F. Wang, H. Duan, M. Tang and H. Jiang, *Nature Energy*, 2018, **3**, 227.
105 W. Gu, A. Magasinski, B. Zdyrko and G. Yushin, *Advanced Energy Materials*, 2015, **5**, 1401148.
106 F. Han, J. Yue, X. Fan, T. Gao, C. Luo, Z. Ma, L. Suo and C. Wang, *Nano Letters*, 2016, **16**, 4521–4527.
107 Z. Lin, Z. Liu, W. Fu, N. J. Dudney and C. Liang, *Angewandte Chemie*, 2013, **125**, 7608–7611.
108 M. Li, Z. Bai, Y. Li, L. Ma, A. Dai, X. Wang, D. Luo, T. Wu, P. Liu, L. Yang *et al.*, *Nature communications*, 2019, **10**, 1–9.
109 T. Swamy, X. Chen and Y.-M. Chiang, *Chemistry of Materials*, 2019, **31**, 707–713.
110 T. Hakari, M. Nagao, A. Hayashi and M. Tatsumisago, *Journal of Power Sources*, 2015, **293**, 721–725.
111 B. R. Shin, Y. J. Nam, D. Y. Oh, D. H. Kim, J. W. Kim and Y. S. Jung, *Electrochimica Acta*, 2014, **146**, 395–402.
112 T. A. Yersak, T. Evans, J. M. Whiteley, S.-B. Son, B. Francisco,

K. H. Oh and S.-H. Lee, *Journal of the Electrochemical Society*, 2014, **161**, A663–A667.

113 X. Li, J. Liang, J. Luo, C. Wang, X. Li, Q. Sun, R. Li, L. Zhang, R. Yang, S. Lu *et al.*, *Advanced Materials*, 2019, **31**, 1808100.

114 S. Ohno, R. Koerver, G. Dewald, C. Rosenbach, P. Titscher, D. Steckermeier, A. Kwade, J. Janek and W. G. Zeier, *Chemistry of Materials*, 2019, **31**, 2930–2940.

115 R. Xu, J. Yue, S. Liu, J. Tu, F. Han, P. Liu and C. Wang, *ACS Energy Letters*, 2019, **4**, 1073–1079.

116 H. Yan, H. Wang, D. Wang, X. Li, Z. Gong and Y. Yang, *Nano letters*, 2019, **19**, 3280–3287.

117 X. Li, J. Liang, X. Li, C. Wang, J. Luo, R. Li and X. Sun, *Energy & Environmental Science*, 2018, **11**, 2828–2832.

118 X. Yao, D. Liu, C. Wang, P. Long, G. Peng, Y.-S. Hu, H. Li, L. Chen and X. Xu, *Nano letters*, 2016, **16**, 7148–7154.

119 Q. Huang, K. Turcheniuk, X. Ren, A. Magasinski, A. Y. Song, Y. Xiao, D. Kim and G. Yushin, *Nature Materials*, 2019, **18**, 1343–1349.

120 J. Scholz, B. Kayaalp, A. C. Juhl, D. Clemens, M. Froba and S. Mascotto, *ACS Energy Letters*, 2018, **3**, 387–392.

121 D. Gueon, M.-Y. Ju and J. H. Moon, *Proceedings of the National Academy of Sciences*, 2020, **117**, 12686–12692.

122 M. B. Nardelli, J.-L. Fattebert, D. Orlikowski, C. Roland, Q. Zhao and J. Bernholc, *Carbon*, 2000, **38**, 1703–1711.

123 Z. Lin, Z. Liu, W. Fu, N. J. Dudney and C. Liang, *Angewandte Chemie International Edition*, 2013, **52**, 7460–7463.

124 X. Yao, N. Huang, F. Han, Q. Zhang, H. Wan, J. P. Mwizerwa, C. Wang and X. Xu, *Advanced Energy Materials*, 2017, **7**, 1602923.

125 Q. Han, X. Li, X. Shi, H. Zhang, D. Song, F. Ding and L. Zhang, *Journal of Materials Chemistry A*, 2019, **7**, 3895–3902.

126 Y. Zhang, T. Liu, Q. Zhang, X. Zhang, S. Wang, X. Wang, L. Li, L.-Z. Fan, C.-W. Nan and Y. Shen, *Journal of Materials Chemistry A*, 2018, **6**, 23345–23356.

127 Y. Zhang, Y. Sun, L. Peng, J. Yang, H. Jia, Z. Zhang, B. Shan and J. Xie, *Energy Storage Materials*, 2019, **21**, 287–296.

128 C. Li, X. Mu, P. A. van Aken and J. Maier, *Advanced Energy Materials*, 2013, **3**, 113–119.

129 A. Manthiram, X. Yu and S. Wang, *Nature Reviews Materials*, 2017, **2**, 1–16.

130 S. Xia, X. Wu, Z. Zhang, Y. Cui and W. Liu, *Chem*, 2019, **5**, 753–785.

131 S. Chen, J. Zhang, L. Nie, X. Hu, Y. Huang, Y. Yu and W. Liu, *Advanced Materials*, 2021, **33**, 2002325.

132 J. Bae, Y. Li, F. Zhao, X. Zhou, Y. Ding and G. Yu, *Energy Storage Materials*, 2018, **15**, 46–52.

133 H. Xie, Y. Bao, J. Cheng, C. Wang, E. M. Hitz, C. Yang, Z. Liang, Y. Zhou, S. He, T. Li *et al.*, *ACS Energy Letters*, 2019, **4**, 2668–2674.

134 Y. He, S. Chen, L. Nie, Z. Sun, X. Wu and W. Liu, *Nano Letters*, 2020, **20**, 7136–7143.

135 K. B. Hatzell and Y. Zheng, *MRS Energy & Sustainability*, 2021, 1–7.

136 F. Shen, M. B. Dixit, X. Xiao and K. B. Hatzell, *ACS Energy Letters*, 2018, **3**, 1056–1061.

137 Z. Deng, Z. Wang, I.-H. Chu, J. Luo and S. P. Ong, *Journal of The Electrochemical Society*, 2016, **163**, A67–A74.

138 Z. D. Hood, H. Wang, A. S. Pandian, R. Peng, K. D. Gilroy, M. Chi, C. Liang and Y. Xia, *Advanced Energy Materials*, 2018, **8**, 1–7.

139 N. C. Rosero-Navarro, A. Miura and K. Tadanaga, *Journal of Power Sources*, 2018, **396**, 33–40.

140 R. Kanno and M. Murayama, *Journal of the electrochemical society*, 2001, **148**, A742–A746.

141 F. P. McGrogan, T. Swamy, S. R. Bishop, E. Eggleton, L. Porz, X. Chen, Y.-M. Chiang and K. J. Van Vliet, *Advanced Energy Materials*, 2017, **7**, 1602011.

142 L. L. Baranowski, C. M. Heveran, V. L. Ferguson and C. R. Stoldt, *ACS Applied Materials and Interfaces*, 2016, **8**, 29573–29579.

143 Y. Sun, K. Suzuki, K. Hara, S. Hori, T.-a. Yano, M. Hara, M. Hirayama and R. Kanno, *Journal of Power Sources*, 2016, **324**, 798–803.

144 T. Shi, Q. Tu, Y. Tian, Y. Xiao, L. J. Miara, O. Kononova and G. Ceder, *Advanced Energy Materials*, 2020, **10**, 1902881.

145 A. Sakuda, A. Hayashi and M. Tatsumisago, *Scientific reports*, 2013, **3**, 2261.

146 R. Garcia-Mendez, F. Mizuno, R. Zhang, T. S. Arthur and J. Sakamoto, *Electrochimica Acta*, 2017, **237**, 144–151.

147 R. Garcia-Mendez, J. G. Smith, J. C. Neuefeind, D. J. Siegel and J. Sakamoto, *Advanced Energy Materials*, 2020, **5**, 2000335.

148 J. Lau, R. H. DeBlock, D. M. Butts, D. S. Ashby, C. S. Choi and B. S. Dunn, *Advanced Energy Materials*, 2018, **8**, 1800933.

149 K. Lee, J. Lee, S. Choi, K. Char and J. W. Choi, *ACS Energy Letters*, 2018, **4**, 94–101.

150 D. H. Tan, A. Banerjee, Z. Deng, E. A. Wu, H. Nguyen, J. M. Doux, X. Wang, J. H. Cheng, S. P. Ong, Y. S. Meng and Z. Chen, *ACS Applied Energy Materials*, 2019, **2**, 6542–6550.

151 Z. D. Hood, C. Kates, M. Kirkham, S. Adhikari, C. Liang and N. Holzwarth, *Solid State Ionics*, 2016, **284**, 61–70.

152 D. H. S. Tan, A. Banerjee, Z. Chen and Y. S. Meng, *Nature Nanotechnology*, 2020, **15**, year.

153 N. Riphaus, B. Stiaszny, H. Beyer, S. Indris, H. A. Gasteiger and S. J. Sedlmaier, *Journal of The Electrochemical Society*, 2019, **166**, A975–A983.

154 F. J. Simon, M. Hanauer, A. Henss, F. H. Richter and J. Janek, *ACS Applied Materials & Interfaces*, 2019, **11**, 42186–42196.

155 R. Koerver, F. Walther, I. Aygün, J. Sann, C. Dietrich, W. G. Zeier and J. Janek, *Journal of Materials Chemistry A*, 2017, **5**, 22750–22760.

156 N. Riphaus, B. Stiaszny, H. Beyer, S. Indris, H. A. Gasteiger and S. J. Sedlmaier, *Journal of The Electrochemical Society*, 2019, **166**, A975–A983.

157 T. H. Hester, D. E. Castillo and D. J. Goebbert, *Rapid Communications in Mass Spectrometry*, 2013, **27**, 1643–1648.

158 X. Liang, C. Hart, Q. Pang, A. Garsuch, T. Weiss and L. F.

Nazar, *Nature communications*, 2015, **6**, 1–8.

159 Y. Li, X. Wang, H. Zhou, X. Xing, A. Banerjee, J. Holoubek, H. Liu, Y. S. Meng and P. Liu, *ACS Energy Letters*, 2020, **5**, 955–961.

160 Y. Ren, N. Hortance, J. McBride and K. B. Hatzell, *ACS Energy Letters*, 2020, **6**, 345–353.

161 I. Villaluenga, K. H. Wujcik, W. Tong, D. Devaux, D. H. C. Wong, J. M. DeSimone and N. P. Balsara, *Proceedings of the National Academy of Sciences*, 2016, **113**, 52–57.

162 L. L. Baranowski, C. M. Heveran, V. L. Ferguson and C. R. Stoldt, *ACS applied materials & interfaces*, 2016, **8**, 29573–29579.

163 N. Balke, S. Jesse, Y. Kim, L. Adamczyk, I. N. Ivanov, N. J. Dudney and S. V. Kalinin, *Acs Nano*, 2010, **4**, 7349–7357.

164 N. Balke, S. Jesse, Y. Kim, L. Adamczyk, A. Tselev, I. N. Ivanov, N. J. Dudney and S. V. Kalinin, *Nano letters*, 2010, **10**, 3420–3425.

165 A. Morozovska, E. Eliseev, N. Balke and S. V. Kalinin, *Journal of Applied Physics*, 2010, **108**, 053712.

166 S. Yang, B. Yan, J. Wu, L. Lu and K. Zeng, *ACS applied materials & interfaces*, 2017, **9**, 13999–14005.

167 Z. Wang, M. Kotobuki, L. Lu and K. Zeng, *Electrochimica Acta*, 2020, **334**, 135553.

168 N. Boaretto, J. Almenara, A. Mikhalchan, R. Marcilla and J. J. Vilatela, *ACS Applied Energy Materials*, 2019, **2**, 5889–5899.

169 H. Yang and J. Qu, *Extreme Mechanics Letters*, 2019, **32**, 100555.

170 S. Chiang, D. Marshall and A. Evans, *Journal of Applied Physics*, 1982, **53**, 298–311.

171 S. Zekoll, C. Marriner-Edwards, A. O. Hekselman, J. Kasemchainan, C. Kuss, D. E. Armstrong, D. Cai, R. J. Wallace, F. H. Richter, J. H. Thijssen *et al.*, *Energy & Environmental Science*, 2018, **11**, 185–201.

172 L. Zhang, T. Yang, C. Du, Q. Liu, Y. Tang, J. Zhao, B. Wang, T. Chen, Y. Sun, P. Jia *et al.*, *Nature Nanotechnology*, 2020, 1–5.

173 M. Ebner, F. Marone, M. Stampanoni and V. Wood, *Science*, 2013, **342**, 716–720.

174 X. Wu, J. Billaud, I. Jerjen, F. Marone, Y. Ishihara, M. Adachi, Y. Adachi, C. Villevieille and Y. Kato, *Advanced Energy Materials*, 2019, **9**, 1–10.

175 D. Liu, Z. Shadike, R. Lin, K. Qian, H. Li, K. Li, S. Wang, Q. Yu, M. Liu, S. Ganapathy, X. Qin, Q. H. Yang, M. Wagemaker, F. Kang, X. Q. Yang and B. Li, *Advanced Materials*, 2019, **31**, 1–57.

176 H. Jia, X. Li, J. Song, X. Zhang, L. Luo, Y. He, B. Li, Y. Cai, S. Hu, X. Xiao *et al.*, *Nature communications*, 2020, **11**, 1–9.

177 I. Robinson and R. Harder, *Nature materials*, 2009, **8**, 291–298.

178 M. Kodama, S. Komiyama, A. Ohashi, N. Horikawa, K. Kawamura and S. Hirai, *Journal of Power Sources*, 2020, **462**, 228160.

179 J. Sottmann, M. Di Michiel, H. Fjellvåg, L. Malavasi, S. Margadonna, P. Vajeeston, G. B. Vaughan and D. S. Wragg, *Angewandte Chemie International Edition*, 2017, **56**, 11385–11389.

180 W. S. LePage, Y. Chen, E. Kazyak, K.-H. Chen, A. J. Sanchez, A. Poli, E. M. Arruda, M. Thouless and N. P. Dasgupta, *Journal of The Electrochemical Society*, 2019, **166**, A89–A97.

181 C. Dai, C. Li, H. Huang, Z. Wang, X. Zhu, X. Liao, X. Chen, Y. Pan and D. Fang, *Solid State Ionics*, 2019, **331**, 56–65.